https://doi.org/10.5194/gmd-2023-57
Preprint. Discussion started: 27 June 2023

Geoscientific Model Development
Discussions
Open Access

Nonparametric estimation method for river cross-sections with point cloud data from UAV photography

URiver-X version 1.0 -methodology development

Keywords: Nonparametric, UAV, Regression, Point Cloud, River, Cross Section

Taesam Lee[1], Jaewoo Park[1], Sunghyun Hwang[1], and Vijay P. Singh[2]

[1] Department of Civil Engineering, Gyeongsang National University,
501 Jinju-daero, Jinju, Gyeongnam, South Korea, 52828

[2] Department of Biological and Agricultural Engineering & Zachry Department of Civil Engineering, Texas A&M University, 321 Scoates Hall, College Station, Texas, United States, 77843; National Water and Energy Center, UAE University, Al Ain, UAE

Corresponding Author :

Taesam Lee, Ph.D.
Gyeongsang National University, Dept. of Civil Engineering
Tel)+82-55-772-1797, Fax)+82-55-772-1799
Email) tae3lee@gnu.ac.kr

https://doi.org/10.5194/gmd-2023-57
Preprint. Discussion started: 27 June 2023

Geoscientific Model Development Discussions
Open Access

Abstract

Aerial surveying with unmanned aerial vehicles (UAVs) has been popularly employed in river management and flood monitoring. One of the major processes in UAV aerial surveying for river applications is to demarcate the cross-section of a river. From the photo images of aerial surveying, a point cloud dataset can be abstracted with the structure from motion technique. To accurately demarcate the cross-section from the cloud points, an appropriate delineation technique is required to reproduce the characteristics of natural and manmade channels, including abrupt changes, bumps, and lined shapes. Therefore, a nonparametric estimation technique, called the K-nearest neighbor local linear regression (KLR) model, was tested in the current study to demarcate the cross-section of a river with a point cloud dataset from aerial surveying. The proposed technique was tested with synthetically simulated trapezoidal, U-shape, and V-shape channels. In addition, the proposed KLR model was compared with the traditional polynomial regression model and another nonparametric technique, locally weighted scatterplot smoothing (LOWESS). The experimental study was performed with the river experiment center in Andong, South Korea. Furthermore, the KLR model was applied to two real case studies in the Migok-cheon stream on Hapcheon-gun and Pori-cheon stream on Yecheon-gun and compared to the other models. With the extensive applications to the feasible river channels, the results indicated that the proposed KLR model can be a suitable alternative for demarcating the cross-section of a river with point cloud data from UAV aerial surveying by reproducing the critical characteristics of natural and manmade channels, including abrupt changes and small bumps as well as different shapes. Finally, the limitation of the UAV-driven demarcation approach was also discussed due to the penetrability of RGB sensors to water.

https://doi.org/10.5194/gmd-2023-57
Preprint. Discussion started: 27 June 2023

Geoscientific Model Development Discussions

1. Introduction

Unmanned aerial vehicles (UAVs) have been popularly employed in recent years, especially to investigate and survey earth systems, such as agriculture and coastal areas (Hugenholtz et al., 2013; Lin et al., 2018; Marfai et al., 2019; Remondino et al., 2011; Siebert and Teizer, 2014; Srivastava et al., 2020; Taddia et al., 2021; Wang et al., 2019; Watanabe and Kawahara, 2016; Yan et al., 2021). Furthermore, river management and fluvial networks have received considerable attention for UAV applications (Gracchi et al., 2021; Langhammer, 2019; Lee et al., 2019; Sanhueza et al., 2019; Tomsett and Leyland, 2019). Additionally, flood monitoring and assessment are one of the major fields in which UAV aerial surveying data have been used (Anders et al., 2020; Andreadakis et al., 2020; Izumida et al., 2017; Kaewwilai, 2019; Perks et al., 2016; Zakaria et al., 2018).

For example, Andreadakis et al. (2020) employed a combination of Structure from Motion (SfM) and optical granulometric techniques in estimating peak discharge and illustrated that the combined UAV technique accurately determined peak discharge. Anders et al. (2020) tested different flying altitudes and area coverage orientations in semiarid and medium-relief areas with respect to cell size and vertical and horizontal accuracy. Perks et al. (2016) applied a novel algorithm to track features associated with free-surface velocity and to allow accurate geometric correction of velocity vectors.

The SfM technique produces 3D information from overlapping images, where the structure refers to the relative parameters of aerial surveying, such as camera positions and focal lengths, and the relative positions of the corresponding features, while the motion refers to the movement of the camera (Javernick et al., 2014; Marteau et al., 2017; Smith et al., 2014). A

https://doi.org/10.5194/gmd-2023-57
Preprint. Discussion started: 27 June 2023

Geoscientific Model Development Discussions

dense point cloud can be determined from the SfM. These point clouds are converted from an arbitrary coordinate system to a geographical coordinate system with camera position and focal length information or by associating reference points on the ground, called ground control points (GCPs), with known coordinates. A point cloud is a set of 3-dimensional points located in space. The 3D locations of a point cloud can be determined from a sensor by emitting pulses and calculating them with the position of the sensor and the pulse direction. Here, the sensor refers to a photogrammetry camera in the current study.

In UAV aerial surveying applications for river management and flood analysis, the demarcation of cross-section of a river is critical. Accurate demarcation of the cross-section is mostly required to calculate peak discharge and flow amount. However, the dense cloud point dataset obtained from UAV aerial surveying and the SfM technique mostly contains errors and does not provide direct cross-sectional information. An appropriate technique to demarcate the cross-section from the point cloud dataset is necessary to develop.

The demarcation of the cross-section in a river has been mostly made with a digital elevation model (DEM) in the literature (Gichamo et al., 2012; Petikas et al., 2020a, b; Pilotti, 2016). For example, Petikas et al. (2020b) proposed a novel method to automatically extract river cross-sections from a DEM along with a parametric cross-section extraction algorithm. However, a cross-sectional algorithm for the cloud point dataset of UAV aerial surveying has not been tested in depth, since the characteristics of the point cloud dataset are far different from the DEM in that a study area for UAV aerial surveying is commonly smaller and many more points can be acquired from UAV aerial surveying.

https://doi.org/10.5194/gmd-2023-57
Preprint. Discussion started: 27 June 2023

Therefore, the current study proposes a demarcation technique for river cross-sections from the point clouds of UAV aerial surveying especially in a small study area. For example, about 80% of national rivers and over 40% of local rivers are maintained by the construction of dikes and revetments for flood control in South Korea. The shape of manmade rivers is mostly trapezoidal due to the stability and easy discharge. A cross-section of manmade rivers also often contains abrupt changes and small bumps as well as smooth variations from aging in natural rivers. The demarcation technique must reproduce the characteristics of manmade channels as well as the ones of typical rivers from aging in natural channels. The proposed demarcation model based on the KLR model was tested to determine whether to reproduce those characteristics.

2. Mathematical Description

With the point cloud data obtained from UAV aerial surveying and postprocessing, the river cross-section must be demarcated. Polynomial regression can be simply applied to the point data. However, a fixed function of the polynomial regression with a few parameters is limited to the highly varied shape of the cross-section. Therefore, a nonparametric regression approach is adopted in the current study, especially K-nearest neighbor local regression (KLR). The KLR model was originally developed by Lee et al. (2017) to predict and simulate hydrologic variables describing a non-linear and hetroscedasticity relationship (non-constant variance of a predictand along with a predictor). The model also presents a strong interpolation ability, especially with a large number of datasets. Therefore, the KLR model was applied to the demarcation of a river cross-section, since the UAV aerial surveying and photogrammetry produce a large number of cloud points and the elevation of a river cross-section is highly non-linear. The KLR model was compared to a parametric model (polynomial regression) and another nonparametric model (LOcally WEighted Scatterplot Smoothing, LOWESS). A detailed description of polynomial

https://doi.org/10.5194/gmd-2023-57
Preprint. Discussion started: 27 June 2023

Geoscientific Model Development Discussions

regression and the proposed nonparametric regression model (KLR) is shown as well as the comparable nonparametric model, LOWESS.

2.1. Polynomial Regression

A polynomial regression model can be used when the relationship between a predictor (x) and an explanatory variable (y) is nonlinear or curvilinear. The Mth-order polynomial regression can be expressed as

$$y = \beta_0 + \beta_1 x + \beta_2 x^2 + \cdots + \beta_k x^M + \epsilon = \sum_{i=0}^{M} \beta_i x^i + \epsilon = \mathbf{x\beta} + \epsilon \tag{1}$$

where ϵ is considered to be a random noise with zero mean and M is the degree of the polynomial regression model, called PolyFit. Here, x can be the distance from the base location in a river cross-section with a length unit (meter, in the current study) and y is the elevation with the same length unit (meter as well).

According to its degree M, the model is structured as follows.

$$y = \beta_0 + \beta_1 x + \beta_2 x^2 + \epsilon \tag{2}$$

$$y = \beta_0 + \beta_1 x + \beta_2 x^2 + \beta_3 x^3 + \epsilon \tag{3}$$

$$y = \beta_0 + \beta_1 x + \beta_2 x^2 + \beta_3 x^3 + \beta_4 x^4 + \epsilon \tag{4}$$

The models in Eq. (2), Eq. (3), and Eq. (4) are defined as PolyFit2, PolyFit3, and PolyFit4, respectively, and employed in the current study.

2.2. KNN-based Local Linear Regression (KLR)

It is assumed that the current condition of the predictor x_t and its corresponding predictand y_t with the observed data (or cloud point data) pairs (x_i, y_i), for $i = 1,\ldots,n$, is given for the n number

https://doi.org/10.5194/gmd-2023-57
Preprint. Discussion started: 27 June 2023

Geoscientific Model Development
Discussions

of data points (i.e., the selected cloud points). In the current study, the pair (x_i,y_i) refers to the observed data of x-coordinate (i.e. distance from the base location) and its corresponding elevation of y-coordinate for the i^{th} observed data (or cloud point data). Note that the base location refers to the point that the x-coordinate of a cross-section begins. The number of neighbors (k) is also assumed to be known. The predictand Y_t is estimated (i.e. the predicted elevation with the length unit, meter in the current study) with the target x_t distance according to the following steps:

(a) Estimate the distances between the current and observed (here, point cloud data) states of the predictors for all n observations as follows:

$$D_j = \left(x_j - x_t\right)^2 \qquad j=1\ldots, n \tag{5}$$

(b) Store the location indices for the k smallest distances.

(c) Fit the local linear regression to the observed dataset of the selected location indices [$x_{(p)}$, $y_{(p)}$] for $p = 1,\ldots,k$, where (p) indicates the p^{th} decreasing ordered location index relative to the distance measure in step (a).

(c-1) Build the weight matrix using the simple selection weight as follows:

$$\boldsymbol{W}_{KLR} = diag\left[\frac{1}{\delta}, \frac{1/2}{\delta}, \ldots, \frac{1/k}{\delta}\right] \tag{6}$$

where $\delta = \sum_{p=1}^{k} 1/p$.

$$\overleftrightarrow{\mathbf{X}}_t = \begin{pmatrix} 1 & x_t - x_{(1)} \\ 1 & x_t - x_{(2)} \\ 1 & \vdots \\ 1 & x_t - x_{(k)} \end{pmatrix} \tag{7}$$

https://doi.org/10.5194/gmd-2023-57
Preprint. Discussion started: 27 June 2023

(c-3) Estimate the parameter vector $\widehat{\boldsymbol{\beta}}_t^{KLR}$ with the weighted least square estimator from the weight matrix $\mathbf{W}_{KLR}$ in Eq. (6) as

$$\widehat{\boldsymbol{\beta}}_t^{KLR} = (\overleftrightarrow{\mathbf{X}}_t^{T} \boldsymbol{W}_{KLR} \overleftrightarrow{\mathbf{X}}_t)^{-1} \overleftrightarrow{\mathbf{X}}_t^{T} \boldsymbol{W}_{KLR} \mathbf{y}_{KLR} \tag{8}$$

where $\mathbf{y}_{KLR}$ is the corresponding predicted value for the ordered observations $[y_{(1)}, y_{(2)}, \dots, y_{(k)}]^T$.

(d) Estimate the current predictor as follows:

$$y_t = \vec{\mathbf{x}}_t^T \widehat{\boldsymbol{\beta}}_t^{KLR} \tag{9}$$

where $\vec{\mathbf{x}}_t = (1 \quad x_t)$.

(e) Repeat steps (a)-(d) until the required data are simulated.

For selecting the number of neighbors k, a heuristic approach for estimating k for the KNNR model is given by $k = \sqrt{n}$ (Lall and Sharma, 1996; Lee and Ouarda, 2011; Lee et al., 2010). Therefore, Lee et al. (2017) suggested a heuristic approach for KLR in which they suggested that the multiplier be

$$k = a\sqrt{n} \tag{10}$$

where a is a multiplier and is a positive integer (i.e., 1, 2, 3, 4).

As noted, only the partial dataset is employed for the observations rather than the whole observation dataset, unlike other regressions. For the point cloud dataset from UAV photography, this proposed approach in the current study is highly advantageous, since the neighboring data

https://doi.org/10.5194/gmd-2023-57
Preprint. Discussion started: 27 June 2023

Geoscientific Model Development Discussions
Open Access

point is sufficient and the fitting of the target point must not be affected by the points that are far away from the target point. This advantage is further discussed in the result section.

2.3. LOcally WEighted Scatterplot Smoothing (LOWESS)

LOWESS was proposed by Cleveland (1979) as a nonparametric regression. The LOWESS with one explanatory variable (x_t, the distance from the base location for x-coordinate) and one predictor variable (y_t, the elevation of the corresponding t^{th} point) can be defined as

$$y_t = m(x_t) + \varepsilon_t \tag{11}$$

where the regression curve $m(\mathbf{y}_t)$ is the conditional expectation $m(x_t) = E(Y|X = x_t)$. The LOWESS estimate can be defined as

$$\widehat{m}_{LOWESS}(x_t) = \vec{x}_t^T \widehat{\boldsymbol{\beta}}_t^{LOWESS} \tag{12}$$

where

$$\widehat{\boldsymbol{\beta}}_t^{LOWESS} = (\overleftrightarrow{\mathbf{X}}_t^T \boldsymbol{W}_t \overleftrightarrow{\mathbf{X}}_t)^{-1} \overleftrightarrow{\mathbf{X}}_t^T \boldsymbol{W}_t \mathbf{y} \tag{13}$$

with

$$\overleftrightarrow{\mathbf{X}}_t = \begin{pmatrix} 1 & x_t^1 - x_1^1 \\ 1 & x_t^1 - x_2^1 \\ 1 & \vdots \\ 1 & x_t^1 - x_n^1 \end{pmatrix} \tag{14}$$

and

$$\boldsymbol{W}_t = \boldsymbol{H}^{-1} diag[K_d(\boldsymbol{H}^{-1}(\boldsymbol{x}_t - \boldsymbol{x}_1)), \cdots, K(\boldsymbol{H}^{-1}(\boldsymbol{x}_t - \boldsymbol{x}_n))] \tag{15}$$

https://doi.org/10.5194/gmd-2023-57
Preprint. Discussion started: 27 June 2023

Geoscientific Model Development Discussions

with the bandwidth matrix, **H**. The major characteristic of LOWESS is to employ the following kernel function:

$$K_d(z) = \begin{cases} (1 - |z|^3)^3 & |z| < 1 \\ 0 & \text{otherwise} \end{cases} \tag{16}$$

https://doi.org/10.5194/gmd-2023-57
Preprint. Discussion started: 27 June 2023

Geoscientific Model Development
Discussions

2.4. Distance Measurement of the Point Cloud

The point cloud data from UAV photography are presented with Transverse Mercator (TM) projection for x, y, and z. The TM projection is a conformal projection presented by Lambert in 1772. To demarcate a cross section of a river, the point cloud data must be projected to a new coordinate system.

As an example in Figure 1, the new coordinate system can be based on the line that connects N and L points presented with the thick red line in Panel (a). The extended thick red line is designated as the new x-coordinate, as shown in Panel (b), and the same z-axis can be defined as the original TM data. The y-coordinate can be chosen as the axis that is perpendicular to the x-coordinate. Let it be assumed that point M, as in Panel (b), is selected among the selected point clouds contained in the NL line. Note that the thick red line in Panel (a) is a group of selected points from the point cloud data for defining the cross-section of the river, as shown in Panel (b).

All of the selected red points must be aligned according to the distance from the datum point (here, N) with the new coordinate system. The new distance for the new x-coordinate can be defined as *k*, as shown in Panel (c). This distance is estimated with the following equations.

The distances of *l*, *m*, and *n* with the TM coordinate can be estimated as follows. For example, $N_{TM}(x)$ represents the x-coordinate of the TM projection for point *N*:

$$l = \sqrt{\left(N_{TM}(x) - M_{TM}(x)\right)^2 + \left(N_{TM}(y) - M_{TM}(y)\right)^2} \quad (17)$$

$$m = \sqrt{\left(N_{TM}(x) - L_{TM}(x)\right)^2 + \left(N_{TM}(y) - L_{TM}(y)\right)^2} \quad (18)$$

https://doi.org/10.5194/gmd-2023-57
Preprint. Discussion started: 27 June 2023

$$n = \sqrt{\left(L_{TM}(x) - M_{TM}(x)\right)^2 + \left(L_{TM}(y) - M_{TM}(y)\right)^2} \quad (19)$$

From the calculated angle of MNL (Θ) in Eq. (24), the new x-coordinate distance (k) can be calculated as in Eq. (25) with the law of cosines (i.e., $n^2 = l^2 + m^2 - 2lmcos\theta$) as the following:

$$cos\theta = \frac{l^2 + m^2 - n^2}{2lm} \quad (20)$$

$$k = l\ cos\theta \quad (21)$$

3. Simulation Study

The performance of the KLR model in fitting the point cloud data for river cross-sections is tested with the simulated point cloud data.

3.1. Model Description and Fitting

A manmade river cross-section is generally trapezoidal due to maximum discharge and easy construction (Chow, 1959). Therefore, a trapezoidal channel was assumed with a 4 m top at both sides and a 6 m base width as well as a 1:1 side slope with a 6 m height, as shown by the thick solid blue line of Figure 2. The channel points were assumed to be measured with 0.1 m intervals, for a total of 161 points. It is assumed that these points work as cloud points that UAV cameras might capture in aerial surveying. The assumed cloud point dataset was generated based on the assumed 161 points (see the thick solid blue line in Figure 3), as follows:

$$Z = Y + \varepsilon \quad (22)$$

https://doi.org/10.5194/gmd-2023-57
Preprint. Discussion started: 27 June 2023

where Y is the assumed points, and $\varepsilon \sim N(0, \sigma_\varepsilon^2)$, i.e., normally distributed error. Note that the generated data (Z) are presented with red circles in Figure 2.

In the current study, σ_ε^2=0.2 was used following similar variability of observed data after testing several values. The magnitude of this error variance (σ_ε^2) represents the differences in the photo locations for the same cloud point of the real ground location (i.e., Y in this case). High variance indicates that extracted point clouds include high errors, and vice versa.

In Figure 2 and Figure 3, the simulated data are presented with red circles. The number of synthetically simulated data points was chosen to be 2 times and 10 times the assumably measured 161 points that were applied for the assumable measured trapezoid line (i.e., 322 and 1610 points), as shown in Figure 2 and Figure 3, respectively. Note that the recommended overlap is 70–80% frontal and 60% side in general cases. In this overlapping case, each cross-section point might be captured approximately 10 times. Therefore, the number of simulated data points is set to 10 times the number of trapezoidal channel points (a total of 1610), as shown in Figure 3. Additionally, there are some portions in which overlapping might not be achieved. The minimal overlap to be a point cloud is at least 2 times, and 2 times the channel points were also tested, as shown in Figure 2.

3.2. Simulation Results

In Figure 2, the fitted cross-section line to the KLR model is shown with the dashed black line for the generated data case with 2 times the assumed target points, while the simulated data are presented with the red circles as noted. Note that the multiplier (a) for the number of nearest neighbors as in $k= a\sqrt{n}$ in Eq. (10) was tested in this figure. As shown in Figure 2, the multiplier a= 1, 2, 3, 4 is shown in each panel. The fitted KLR line with a smaller multiplier presents more

https://doi.org/10.5194/gmd-2023-57
Preprint. Discussion started: 27 June 2023

Geoscientific Model Development Discussions Open Access EGU

irregularity, while the line with a higher multiplier appears to be smooth. For example, the top part of the trapezoid channel with the 22 m of the y-coordinate shows that the KLR line with the multiplier a=1 (the panel(a) of Figure 2) was drawn rather coarse, but the straight shape of the original channel is preserved. At the same time, the fitted line with the high multiplier a=4 (Panel (d) of Figure 2) presents a very smooth feature and presents the original top and bottom horizontal parts, which are rather too curved.

The multipliers of a=2 and 3 in the fitted KLR model, as shown (Panels (c) and (d) of Figure 2), appear to mix the smooth and horizontal features well by fitting the top and bottom horizontal lines, and the angled part of the original channel is reproduced well. This finding indicates that an appropriate multiplier (a in Eq. (10)) is required to present the straight and angled trapezoid channel better.

This characteristic continues to be the case with the high number of captured cloud points, as shown in Figure 3 (i.e., 10 times the target points, for a total of 1610 points, as shown with the red circles in this figure). It is comparable to the case of 2 times the target points in Figure 2 in that all of the fitted line with the KLR model with the case of 10 times presents better the original trapezoid channel than the case of 2 times. It is obvious that a higher number of points can significantly improve the quality of the KLR model, since the nonparametric KLR model directly applies the observed data and its performance highly depends on the number of data points. In other words, while parametric models, such as linear regression and polynomial regression, estimate the parameters from the data and the parameters are employed, the nonparametric KLR model employs the data itself directly to estimate the cross-section. It can be appreciated that the UAV aerial photography usually captures a large enough number of points to produce overlapping points as many as 10 times the target points.

https://doi.org/10.5194/gmd-2023-57
Preprint. Discussion started: 27 June 2023

Geoscientific Model Development
Discussions

The horizontal and angled trapezoid shape (i.e., the solid thick blue line in Figure 3) is reproduced well by the KLR model (see the dashed black line), even though a coarse zig-zag line is still observed in the case of the small multiplier (i.e., *a*=1, see Panel (*a*) of Figure 3). Also, the angled portion is too curved in the case of the high multiplier (i.e., *a*=4, see Panel (*d*) of Figure 3).

The results of Figure 2 and Figure 3 illustrate that a value between 2 and 3 can be a good selection for the multiplier. Further testing was performed to select the multiplier for the number of nearest neighbors by varying the multiplier from 0.5 to 5.0 with a 0.5 interval. The root mean square error (RMSE) and the mean absolute error (MAE) were estimated as

$$RMSE = \sqrt{\frac{1}{\mathrm{N}}\sum_{t=1}^{N}\left(y_t - Y_t^{model}\right)^2} \quad (23)$$

$$MAE = \frac{1}{\mathrm{N}}\sum_{t=1}^{N}\left|y_t - Y_t^{model}\right| \quad (24)$$

where Y_t^{model} is the estimate from a model like the KLR in Eq. (9), and y_t represents the original points with N trapezoid points (here, 161 points).

The RMSE results of the KLR estimate with different multipliers (i.e., *a* in Eq. (10)) are shown in Figure 4 for the case of 2 times (top panel) the original trapezoidal points and the case of 10 times (bottom panel). In the 2 and 10 times cases, the optimum multiplier (i.e., the smallest multiplier *a*) can be selected to be between 1.5 and 2.5. To fully reveal the characteristics of the multiplier with multiple simulations, all of the multiple simulations from 1 to 12, indicating the number of overlapped photos, were tested while finding the optimum multiplier. The result in Figure 5 shows that a smaller optimum multiplier is selected with a smaller number of overlapped photos (or multiple simulation points) as much as 1.5–2.0, and vice versa as much as

https://doi.org/10.5194/gmd-2023-57
Preprint. Discussion started: 27 June 2023

2.0–2.5. Since the number of overlapping photos might be difficult to know and each point does not have the same number of points in real UAV aerial survey, the multiplier is suggested to be 2.0 in the current study.

To compare other approaches to fit the point cloud in demarcating the cross-section of a river, polynomial regression and locally weighted scatterplot smoothing (LOWESS) were also tested. The result is presented in the top and bottom panels of Figure 6 and Figure 7 for the fitted line to the polynomial regression (top panel) and the LOWESS model, respectively. The fitted line to the polynomial regression of 2^{nd} degree (see the thick dash-dotted black line with the circle marker in the top panel of Figure 6 and Figure 7) does not reproduce the top and bottom horizontal lines of the trapezoid channel well. Better performance in the 4^{th} degree polynomial regression model is presented (see the dotted black line with the reverse triangle marker). However, the depth of the trapezoid center is overestimated. Other degrees of polynomial regression models were also tested, but no better performance was observed.

Furthermore, the LOWESS model was additionally fitted to the simulated trapezoid channel data. Note that the LOWESS model is also a nonparametric regression model as described already. The major difference between the LOWESS model and the KLR model is that the LOWESS model includes all of the observed data in the estimate, as shown in Eqs. (13) and (14), while the KLR model includes only the k-nearest neighbor observations, as in Eq. (7). The performances of the LOWESS and KLR models were compared in detail in Lee et al. (2017) for the heteroscedastic relation of time series data. The result in the study of Lee et al. (2017) indicated that the KLR model reproduced an abrupt change in the heteroscedastic relation. The results of the LOWESS model are presented in the bottom panels of Figure 6 and Figure 7. The

Geoscientific Model Development Discussions
Open Access

results indicate that the bottom part of the trapezoidal channel is reproduced well with the LOWESS model. However, the model does not reproduce the abruptly curved area well.

3.3. Simulation tests with V-shape and U-shape cross-sections

In order to further test the performance of the proposed KLR model, two additional shapes of cross-sections as U- and V-shape were tested. The U-shape channel was included, since most of natural channels present this shape and the V-shape channel can be either manmade or natural.

3.3.1. U-shape cross-section

The U-shape cross-section that is close to a natural river was tested. The U-shape cross was modelled with a power function from Neal et al. (2015) as

$$w_f = w_F \left(\frac{h_f}{h_F}\right)^{\frac{1}{s}} \quad (25)$$

$$h_f = h_F \left(\frac{w_f}{w_F}\right)^{s} \quad (26)$$

where w_f indicate the flow width, while w_F is the bank-full flow width and h_f and h_F is the height of flow width and the height in a bank-full condition, respectively. Also, s is the parameter to vary the shape of the cross-section. Here, s=5 was set as used in Neal et al. (2015) as a basic value. To design a similar bank to the trapezoid model in the previous test, h_F=5m and w_F=20m was used. The number of points for the U-shape cross-section is divided to 262 points including the flat river bank and the designed cross-section was presented in a blue solid line with cross markers as shown in Figure 8. The synthetic point cloud data was simulated with Eq.(11) and the number of point clouds was 10 times of the U-shape cross-sections (i.e. 2620 points), shown with the red dots in Figure 8.

https://doi.org/10.5194/gmd-2023-57
Preprint. Discussion started: 27 June 2023

Geoscientific Model Development Discussions

This designed U-shape cross-section was fitted to the proposed KLR model and the other models as LOWESS and PolyFit, as shown in Figure 8. Note that a=2 (see Eq.(10)) was applied for the KLR model from the result of the trapezoid case. The result in Figure 8 indicates that the KLR model reproduces well the U-shape cross-section without any deviation. Meanwhile, the LOWESS model fitted U-shape cross-section well in the middle part, but the connected part (between 4m and 6m of x-coordinate) of the U-shape cross-section was not fitted well. The PolyFit model fairly fitted the U-shape cross-section with the 4th model (i.e. PolyFit4) except slight deviation in the connected area between the slope and top bank. The PolyFit2 and PolyFit3 models were poorly performed due to its limit of the flexibility.

3.3.2. V-shape cross-section

One of the unique shape of cross-sections is the V-shape for a river cross-section. The V-shape weir (or triangle shape, v-notch) was often built to provide a highly accurate solution for open channel flow measurement. Also, the V-shape river cross-section can be developed naturally when the sides are cut down and attacked by weathering. In addition, the loosened material slowly creeps down the slope by gravity. A V-shape cross-section was synthetically designed as shown in Figure 9 with the height of 4m and the top width of 16m so that the slopes of both sides are in 1:2. The cross-section was divided to 121points, including the flat river bank shown with the blue solid line with cross markers in Figure 9 and 10 times of the points was synthetically generated for point cloud data with Eq. (11) and presented with the red dots.

The point cloud data was fitted to KLR, LOWESS, and PolyFit models and shown in the panels (a), (b) and (c) of Figure 9, respectively. Here, a=2.0 was also employed for the KLR model. The result of the KLR model indicates that the V-shape cross-section also was fitted well by the KLR model with a minimal deviation at the acute angle bottom section. Meanwhile, the

https://doi.org/10.5194/gmd-2023-57
Preprint. Discussion started: 27 June 2023

LOWESS model highly deviated at the acute bottom section and slight deviation was present at the top connected part. The PolyFit model did not fairly fit the V-shape model even with PolyFit4. Further higher order model was tested (i.e. PolyFit5 and PolyFit6) and no improvement was found with increasing the order for the PolyFit model.

Table 1 presents the estimated RMSE and MAE for three tested models of KLR, LOWESS, and PolyFit4 with trapezoidal, U-shape, and V-shape cross-section data. Note that only PolyFit4 was presented, since 4^{th}-degree was the best for the PolyFit models. The RMSE and MAE estimates present that the KLR model outperforms the other fitting models, while the other two models of PolyFit4 and LOWESS are comparable to each other for trapezoidal and U-shape cross-sections. For V-shape channel, the LOWESS much better performed than the PolyFit4, since the PolyFit4 is a parametric model that connects the points rather smoothly and abrupt change cannot be modelled well due to its limited flexibility. Overall, the simulation study indicates that the proposed KLR model is a good alternative to demarcate the different shape cross-sections.

Further, nonparametric models and other regression models, such as logistic regression (Ahmad et al., 1988; Elek and Márkus, 2004; Orlowsky et al., 2010; Simonoff, 1996), can be tested. However, the simulation study with the trapezoid channel that is similar to the real river cross-section shows that the presented KLR nonparametric model originally developed by Lee et al. (2017) is suitable for demarcating the cross-section of a river. The major reason for the good performance is that the KLR model employs only k-nearest neighbor observations. This approach might not be beneficial, when an overall trend is needed, and not enough observations are available. However, the point cloud data taken from UAV aerial surveying often provides a large enough number of points in the data set. Furthermore, the cross-sections in a manmade river can contain irregularity and abrupt changes by river aging. This feature can be captured only through fitting nearby observations. Therefore, the KLR model might be a suitable alternative to demarcating the cross-section of a river with the cloud point dataset.

4. Experimental Study

4.1. Experimental Site

In order to validate the performance of the proposed KLR model, the River Experiment Center (REC) in Korea Institute of Civil Engineering and Building Technology was selected as an experimental site (Lee et al., 2022), as shown in Figure 10. The REC consists of a total area 193,051 m^3 with three rivers of open channels with a length of 560~680 m, width of 11 m, and depth of 2 m. The three channels are (1) the steep river (U-shape), (2) the meandering river (S-shape), and (3) the straight river (I-shape) as shown in the bottom panel of Figure 10. The steep river (U-shape) with a length of 590 m has a slope of 1.4% and its flow can have a velocity up to 5.0 m/s in the upstream to test the stability of bank revetment. The slope of the downstream at the steep river is 0.125% and is employed for hydraulic experiments, including vegetation development over the banks and sediment transport in the river bed. The straight river (I-shape) with a length of 560 m has a low-slope and it contains concrete compound for international cooperation study. The meandering river (S-shape) of the REC with a length of 682m has a 1.2~1.7 sinuosity that can be employed for various experiments, including pollutant dispersion and flow structures.

On each river, six to seven cross-sections were selected, as shown in the bottom panel of Figure 10, to test the demarcation method of the current study. The channels were ground-surveyed and estimated with the UAV-based demarcation method. The steep river (S-shape) is

https://doi.org/10.5194/gmd-2023-57
Preprint. Discussion started: 27 June 2023

Geoscientific Model Development Discussions

located at the bottom and 7 cross-sections were surveyed as U_1, U_2,..., and U_7. The straight river (I-shape) is in the middle among three rivers with 6 cross-sections as I_1,.., and I_6. The meandering river (S-shape) is placed at the top and 7 cross-sections were tested as S_1, S_2,..., and S_7.

4.2. Application Methodology

4.2.1. Ground Surveying

For comparing demarcation methods, the real ground points were surveyed using the Global Positioning System (GPS). The EMLID Reach RS2 with centimeter precision was used for GPS surveying, as shown in panels (a) and (b) of Figure S3 of the Supplementary Material. At each channel point, about 10~15 points from the three rivers in the REC were surveyed with the GPS system.

4.2.2. UAV Aerial Surveying

For aerial surveying of the REC, the Autel Evo II shown in the panel (c) of Figure S3 of the Supplementary Material was employed with 4000x3000 pixels with the vertical and horizontal resolutions of 96 DPI and 2.41cm of the average ground sampling distance. Note that the XT701 camera was applied with ISO-100 and the 1/2” CMOS. The built-in flight path module of the Autel Evo II in the controller (see the panel (d) of Figure S3) was used to automatically obtain the aerial images of the REC, especially the targeted three experiment rivers. For the UAV photogrammetry of the REC, Pix4D Mapper was employed.

4.3. Experiment Results

In order to improve its accuracy for the UAV aerial surveying, 10 GCPs were employed with ground surveying and 34 check points were estimated for checking the entire accuracy of

https://doi.org/10.5194/gmd-2023-57
Preprint. Discussion started: 27 June 2023

Geoscientific Model Development Discussions

the REC. The RMSE of the GCPs was 0.007m for Z and 0.017m and 0.055m for X and Y. The RMSE of the check points was 0.047m for Z and 0.040 and 0.071 for X and Y. This result indicates that the UAV aerial surveying produced the ground positions of the REC, including the target three rivers and channels. The detailed quality report from the Pix4Dmapper is uploaded in the Mendeley Data respiratory on the website of https://data.mendeley.com/datasets/xdw4cgnvhm/2.

For I_1 in Figure 11, the point cloud (red circles) matched fairly the observed result of ground surveying (blue solid line with x marker) with a slight difference at the edge of the channel bottom in 4m and 8m of the x-coordinate. The KLR shown in the panel(a) of Figure 11 draws the cross-section of I_1 following the point cloud. A similar result can be found with the LOWESS in panel(b) of Figure 11 except that the left-top part of the channel (i.e. around 0 m of the x-coordinate) is not preserved with the LOWESS. The polynomial regression of different degrees, shown in panel(c) of Figure 11, performed very similarly to each other. The method fairly depicted the cross-section of I_1 except for the left-top part of the abrupt change.

The fifth channel of the straight river (I_5) shown in Figure 12 presents two different bottom sections. This type of the channel is common in reality when a river bottom is renovated to use the portion of the river bottom as a playground or a parking place. The observed ground surveying data (blue solid line with x marker in Figure 12) matched well the point cloud (red circles) from the UAV aerial surveying. The KLR method demarcated this channel with two bottom sections in panel(a) of Figure 12, including the abrupt varied part of the bottom (2m, 5m, 7m, and 11m of the x-coordinate) and the top (0m, 1m, and 12m of the x-coordinate). The LOWESS shown in panel(b) of Figure 12 does not depict well the channel, especially in the abrupt changed parts. With the polynomial regression in panel(c) of Figure 12, a higher degree

https://doi.org/10.5194/gmd-2023-57
Preprint. Discussion started: 27 June 2023

Geoscientific Model Development
Open Access
Discussions
EGU

model is needed, since it includes two different bottom sections. Likely, the 4th polynomial model showed the best performance among other degree polynomials. However, the changed part was not reproduced well with any degree polynomial regression model. Similar characteristics can be observed in the other channels for I_2, I_3, I_4, and I_5 shown in Figures S4-S7 of the supplementary material. The RMSE and MAE results of the tested channels are presented in Table 2 and Table 3,. The performance measures reflected the superiority of the KLR model presenting the smallest RMSE and MAE for the channels of the straight river (i.e. I-shape).

The first channel of the steep river (i.e. U_1) is presented in Figure 13 and it has a typical shape of manmade river as presented in the simulation study of section 3 in Figure 2 and Figure 6. The observed data of the ground surveying (blue solid line with x marker) matches well the aerial surveying data of the point cloud (red circles) in Figure 13. The KLR model depicted well this typical trapezoid channel, as shown in panel(a) of Figure 13. Also, the LOWESS and the polynomial regression model depicted this channel with a slight deviation at the angled bottom part (3 m and 7 m in the x-coordinate) presented in panels (b) and (c) of Figure 13, respectively.

The second channel of the steep river (U_2) shown in Figure 14 has a winding bottom. The drawn channel with the ground surveyed data shows that the varied bottom was not surveyed well. The ground surveying of the channel bottom often missed this variation due to its time limit and accessibility. In contrast, the demarcation method with the point cloud of the UAV aerial surveying depicted the detailed winding bottom. The KLR model reproduced this channel shape well, including the winding bottom as shown in panel (a) of Figure 14. The LOWESS also demarcated this channel fairly (see the panel (c) of in Figure 14). However, the polynomial regression did not depict this cross-section well by smoothing too much the winding bottom. Similar result can be observed to the other channels for U_3, U_4, U_5, and U_6 shown in Figures S4-

https://doi.org/10.5194/gmd-2023-57
Preprint. Discussion started: 27 June 2023

S7 of the supplementary material. The performance measures of RMSE and MAE in Table 2 and Table 3, respectively, also showed that the KLR model performed the best for the channels of the steep river with U-shape.

The selected channels for the meandering river (S-shape) are presented in Figure 15 and Figure 16 for S_3 and S_6, respectively. Both channels show the common natural U-shape in the simulation study of section 3.3.1. The 3rd channel of the meandering river is shown in Figure 15 (i.e. S_3). The observed result from the ground surveying showed a slight deviation to the point cloud with the UAV aerial surveying. This deviation is also shown in other channels for the meandering river (S_1, S_2, S_4, S_5, and S_7 shown in Figures S13-S17 of the supplementary material). Locating the exact cross-section might be difficult to measure especially in a meandering river and this location difficulty might result in the deviation. This U-shape channel is depicted fairly with the KLR and LOWESS models (see panels (a) and (b) of Figure 15) as well as the polynomial regression of the 4th degree (panel (c)). The 6th channel of the meandering river (S_6) performed similar to the S_3 with a better representation of the observed result by the point cloud. Note that the natural U-shape channel is demarcated fairly well with all three methods shown in the simulation study. The RMSE and MAE results of the tested channels of the meandering river (S-shape) are presented in Table 2 and Table 3,respectively. The KLR model showed the smallest magnitude for S_1, S_2, S_4, S_5, and S_7. Meanwhile, the performance result for S_3 and S_6 showed that the polynomial regression with the 4th degree presented the best performance in Table 2 and Table 3. Note that some deviation between the observed result and the point cloud data is shown for the meandering river. Also, the S_3 and S_6 channels have the U-shape of the common natural river as discussed in the simulation study and the smooth characteristics of a U-shape channel can be reproduced well with the polynomial regression.

https://doi.org/10.5194/gmd-2023-57
Preprint. Discussion started: 27 June 2023

5. Case Study of Hapcheon

5.1. Study Area and Data Acquisition

5.1.1. Study Area

The study area is located in the Migok-cheon stream flowing through Hapcheon-gun, South Korea, as shown in Figure 17. The Migok-cheon stream has an 8.8 km length and 13.9 km^2 watershed area. The slope of the stream is approximately 1/50~1/400, and the study area has a slope of 1/350. This stream conjuncts to the Hwanggang River at the end of the stream, and the Hwanggang River whose major discharge was made from Hapcheon Dam above is joined into the Nakdong River directly afterward. Therefore, the Migok-cheon stream is highly affected by the water levels of the Hwanggang River. Also, the fundamental engineering plan to prevent floods for the Migok-cheon stream was made in 2004 and the plan was updated in 2019 (BRTMA, 2019).

In the middle of the Hwanggang River, the Hapcheon dam is located for electricity generation and water resources. The upstream Hapcheon River consists of a number of mountains, and the slope is high, producing rapid floods and short concentration times to induce floods. For example, in August 2020, the Hapcheon dam outflowed a large amount of water downstream and induced a high-water level in the Hwanggang River. A number of streams joining the Hwanggang River overflowed due to the high level of the Hwanggang River, including the Migok-cheon stream (Seong et al., 2020). To reduce damage from floods in the area of the Migok-cheon stream, an early warning system for floods is being considered. For the early-warning system for floods, detailed cross-sections of the Migok-cheon stream must be obtained to decide which water level is appropriate for an alarm. In the current study, four sites

https://doi.org/10.5194/gmd-2023-57
Preprint. Discussion started: 27 June 2023

Geoscientific Model Development Discussions
Open Access
EGU

were selected to test the performance of the proposed model located along the Migok-cheon stream as shown in Figure 18. The Naesamhak village is located on the left side of the river, while only cultivation land is on the right side indicating that the left bank has higher importance to water managers. Also, the Unsam bridge is placed in the middle the Migok-cheon stream.

5.1.2. Data Acquisition

Specification of Employed UAV

Aerial photos over the selected Migok-cheon were obtained with the unmanned aerial vehicle (also termed drone), DJI Phantom 4. This UAV is one of the most popular professional drones on the market and contains an advanced stereo vision positioning system that provides precise hovering even without satellite positioning support (Hamdi et al., 2019). The camera applied is FC3411 with ISO-110 and the image sensor of 1/2.3" CMOS, and the images taken from DJI Phantom 4 are 5472x3648 pixels at approximately 10 M with the horizontal and vertical resolutions of 75 DPI. Pix4Dcapture was employed to map the target area. The flight with a height of 75 meters was made on July 08, 2021.

Ground Control Points

Ground control points (GCPs) are the points on the ground that have measured or known coordinates. To obtain GCPs, 10 specific points were measured over the target area on the ground with global positioning system (GPS) surveying. The EMLID Reach RS2 (https://emlid.com/reachrs2/), multiband RTK GNSS receiver, with centimeter precision, was employed for GPS surveying.

https://doi.org/10.5194/gmd-2023-57
Preprint. Discussion started: 27 June 2023

Data Processing (WebODM)

The aerial photos were postprocessed to build a point cloud dataset with WebODM. The WebODM (https://github.com/OpenDroneMap/WebODM) is an open-source tool for generating map point clouds, and terrain and 3D surface models from aerial images.

5.2. Results

5.2.1. Selected sites for cross-section demarcation

The four tested sites in the Migok-cheon stream are presented in Figure 18. The overall produced point cloud dataset for the UAV surveying area is presented in the top-left panel of Figure 18, and the picture of the top-left panel consists of only the collected points. Site-1 is located in the middle of the study area, while Site-2 is in the upper part of the area. Since the nearby area of Site-1 is located in the middle of the UAV surveying coverage, several images can be overleaped and captured for the same points. The other two sites (Site-3 and Site-4) that are located between Site-1 and Site-2 were added for further comparison.

Therefore, the number of points for demarcating a cross-section of the river might be sufficient to capture the detailed characteristics of the cross-section (see the top-right panel of Figure 18) like in Site-1 (see the red dots in Figure 19) as well as Site-3 and Site-4 (see Figure 21 and Figure 22). In contrast, Site-2 is located at the upper part of the coverage area, and overlapping images might be limited, which indicates that the number of points to capture a target cross-section is also limited as shown in the red dots in Figure 20. Furthermore, part of the cross-sectional area can be missing due to technical and environmental limitations, such as waterbodies and insufficient overlapping images as well as shadow from the sun. For example, there are some areas in which no cloud point data exists, as on the right side of Site-2. This point is intentionally selected to verify the model performance in such a case.

5.2.2. Demarcation of selected cross-sections

The demarcated cross-sections for the selected sites (i.e., Site-1, Site-2, Site-3, and Site-4) are illustrated in Figure 19, Figure 20, Figure 21, and Figure 22, respectively. Also, the RMSE and MAE estimates are presented in Table 4 to show the performance of the presented models. In Figure 19, the extracted cloud points for Site-1 are presented with red circles. As noted, a number of cloud points were extracted from the UAV aerial photographs for Site-1, since the site is located with enough photo coverage. The KLR fitted line shown with the dashed black line of the panel (a) of Figure 19 indicates that the fitted line reproduces the characteristics of the natural cross-section of the river well, including the overall trapezoidal shape and the natural bumps at the bottom. This line is compared with field measurements reported in BRTMA (2019). Slight differences can be seen between field measurements (shown with the solid blue line with the x marker) and the KLR fitted line since field measurements took place approximately about 3 years ago.

The LOWESS model and the PolyFit models with the degree of 2, 3, and 4 were also tested and their results were presented in panels (b) and (c) of Figure 19, respectively. The LOWESS fairly fitted the point cloud data except the left side between 14 m and 20 m of the x-coordinate) with deviation from major cloud points. Meanwhile, all the Polyfit models (i.e. 2nd , 3rd , and 4th degrees) did not fit the point cloud data fairly with high deviation from the point cloud.

The cross-section of Site-2 is presented in Figure 20 and shows that the middle part of the left slope of the stream has no cloud point data. The KLR fitted line shows that the overall

https://doi.org/10.5194/gmd-2023-57
Preprint. Discussion started: 27 June 2023

characteristics of the cross-section are reproduced. Even the missing part of the cross-section between 12 m and 17 m of the x-coordinate is also interpolated well with the KLR model by comparing field measurements (see the solid blue line with the x marker in Figure 20). Some differences between the fitted line and the field measurement might result from the year difference. This result indicates that a missing part of the aerial surveying can be filled up with the interpolation of the KLR method. This can be a good benefit of the KLR model in demarcating the cross-sections with the UAV point cloud data, since this missing data can be sometimes inevitable. Otherwise, further UAV surveying might be required to fill up the gap costing additional time and money.

The LOWESS model also fitted fairly well the point cloud data through all the section (see the panel(b) of Figure 20) except that slight deviation can be observable on the right side of the top bank between 40 m and 42 m of x-coordinate. Also, the missing part (between 12 m and 17 m of the x-coordinate) was rather not fairly interpolated with the LOWESS model. This might be induced from the lack of the points in this missing area, since the farther left side has denser points and the predicted points from the LOWESS model might be affected by these dense points. The PolyFit does not estimate the model well due to the lack of the model flexibility to an abrupt change of the cross-sections as mentioned.

Site-3 contains a number of cloud points as shown in Figure 21 . The KLR model well fitted the cloud points while the LOWESS model presents the good performance (see the panel (b) of Figure 21), but the deviation from the cloud points is observed in the left bank section (i.e. between 0 m and 3 m of x-coordinate). The PolyFit4 model as shown in (see the panel (c) of Figure 21) fairly performs in fitting the cloud data points. It is because the shape of the cross-section is rather smoothly curved. The Site-4 result shown in Figure 22 indicates that the KLR

https://doi.org/10.5194/gmd-2023-57
Preprint. Discussion started: 27 June 2023

Geoscientific Model Development Discussions

model (the panel(a)) performs well in fitting the cloud points from the UAV surveying, while the LOWESS model presents significant deviation from the cloud points on the right side and the PolyFit models did not fairly perform.

The performance measures of RMSE and MAE are presented in Table 4 for all four sites and three tested models. The RMSE value of KLR is between 0.32-0.47 while the that of LOWESS and PolyFit is between 0.45-0.94 and 0.71-1.4. This performance result indicates that KLR outperforms the LOWESS and PolyFit models for all four sites. The PolyFit model (RMSE: 0.70 and MAE: 0.76) better performs than does the LOWESS model (RMSE: 0.94 and MAE: 0.83) for Site-4, while LOWESS is always better for other sites. The overall result of the case study indicates that the KLR method can reproduce the characteristics of the cross-section of a natural river and be a good alternative to demarcate a cross-section in a river.

6. Case Study of Yecheon

6.1. Study Area and Data Acquisition

One more case site, the Pori-cheon stream in Yechoen-gun was selected to reveal the performance of the proposed KLR model with the point cloud as shown in Figure 23. Four sites were ground-surveyed with the EMLID Reach RS2 and aerial surveying was also performed with the Autel Evo II. For this site, the same UAV and GPS tool were used as the REC in section 4. The Y1 is located in the upper stream of the Pori-cheon stream than the Y4. The cross-section of Y2 is located in the right below of the bridge followed by the Y3 cross-section. The detailed shape of the cross-section is shown from Figure 24 to Figure 27 for each cross-section. At each section, 10-12 points were ground-surveyed and the point cloud were abstracted

https://doi.org/10.5194/gmd-2023-57
Preprint. Discussion started: 27 June 2023

Geoscientific Model Development Discussions

with Pix4D mapper while the bottom width is about 10m. The demarcation of the cross-section with the tested KLR, LOWESS, and Polyfit models was performed.

6.2. Results

The shape of the Y1 cross-section presents the rough river bottom (Figure 24) while the left section has lower bottom and the section should be major flow passage during low streamflow. The other side of this cross-section has further ups and downs possibly by debris and riparian vegetation. These ups and downs were not measured in detail by ground surveying. Additional ground surveying can capture the characteristic. However, it requires further time consumption for measurement and the accessibility cannot be guaranteed even in such a small stream. Meanwhile, the point cloud captures the detailed characteristics of the channel bottom and KLR model describes the characteristics as shown in the top panel of Figure 24 following the major cloud data. In LOWESS, the Y1 cross-section is not presented with missing the abrupt change in both walls of the cross-section (the middle panel of Figure 24) and all the Polyfit models present similar behavior as the result of the LOWSS. The wall part (5-6m and 17-18m of the cross-section) was not well reproduced by the Polyfit models. The RMSE and MAE in Table 5 present the superiority of the KLR for the Y1 cross-section. The RMSE and MAE of the Y1 is rather larger than the other cross-section. This large error might be induced from the ups and downs of the channel bottom.

Meantime, the Y2 cross-section in Figure 25 shows similar to the U-shape of a natural river in Figure 8. The ground-surveyed points (blue solid line with cross markers in Figure 25) are matched well with the point cloud data except the slight deviation at the left-top embankment (in 2-3m). This U-shape cross-section is demarcated well with the KLR model while slight

https://doi.org/10.5194/gmd-2023-57
Preprint. Discussion started: 27 June 2023

underestimation can be observed with the LOWESS model in the right embankment (13-14m). Not much good performance can be seen with all the Polyfit models shown at the bottom panel of Figure 25. The RMSE and MAE in Table 5 also show the worst performance in the Polyfit models and superiority with the KLR model.

The Y3 and Y4 cross-sections in Figure 26 and Figure 27, respectively, present traditional man-made trapezoid shape. These trapezoid channels were modeled both with KLR and LOWESS while the KLR presents better descriptive characteristics in the abrupt changing part of the cross-section. While the Polyfit-4 presents fair performance to model the Y4 cross-section in Figure 27, the Y3 was not demarcated well with all the Polyfit models. The RMSE of the KLR model is only 0.092 and 0.068 while the LOWESS shows 0.236 and 0.116 for the Y3 and Y4 cross-sections in Table 5. The results indicate that the KLR model presents superiority among all the tested LOWESS and Polyfit models in case of all different shapes as the irregular U-shape, trapezoid-shape channels in the Pori-cheon stream, Yecheon.

7. Discussion

The results of the synthetic simulation study and two case studies as well as the experiment study of the REC site present that the proposed KLR model can demarcate the cross-sections of a river with different shapes. However, there are some limitations and conditions to apply the proposed model in the demarcation of river cross-sections. At first, UAV sensors cannot penetrate water depth unless bathymetric technology is not applied. Currently, river photogrammetry with bathymetry data has been applied to penetrate water body using specialized sensors, such as Light Detection and Ranging (LiDAR), which is called bathymetry LiDAR (Allouis et al., 2010; Fernandez-Diaz et al., 2014). The case study of the current study

https://doi.org/10.5194/gmd-2023-57
Preprint. Discussion started: 27 June 2023

does not use the bathymetry data, since the water depth is very shallow and not critical to illustrate a river cross-section. The proposed KLR model with the point cloud data must be carefully applied to a dry stream or very shallow river with the water surface whose level is ignorable especially for its discharge amount. Otherwise, a bathymetry data must be applied using a special sensor (e.g. bathymetry LiDAR).

Secondly, the KLR model should define the number of K-neighbors. The result of the tested model illustrates that the value of 1.5-2.5 for ‘a’ in Eq. (10) might be a good range. Further estimation procedure might be required in some cases to produce cross-sections that are more accurate. However, the value is not very sensitive at each case presented in the current study. Note that a=2.0 was employed -for the U-shape and V-shape synthetic cross-section and the case study without any further estimation procedure.

Furthermore, traditional ground surveying might be essential to supplement UAV or LiDAR-based point clouds for the purpose of hydraulic modeling due to the penetration capability of sensors and sensitivity even with capable sensors. A ground surveying for a few cross-sections can be performed in addition to UAV surveying. The ground-surveyed cross-sections can be employed to validate the UAV-based cross-sections. This additional ground surveying might improve much the quality of the UAV-based cross-sections.

The UAV-based demarcation of cross-sections still has some limitations and conditions to ensure its credibility, such as water penetration and additional requirement of ground surveying Nevertheless, the proposed KLR model can be applicable to the demarcation of different cross-section shapes with UAV point cloud data. In addition, UAV sensors and photogrammetry technology have been developed so that the current KLR method might be more useful and applicable with UAV-based data. UAV surveying can be a potential surrogate for its relatively

https://doi.org/10.5194/gmd-2023-57
Preprint. Discussion started: 27 June 2023

cheap and time-saving. The river cross-section with UAV surveying can be beneficial when the ground surveying cannot be made. After initial ground surveying, further resources may not be available for additional ground surveying. In this case, the river cross-section with UAV surveying can extract any places inside the surveyed area.

8. Summary and Conclusions

The current study presents a nonparametric fitting method, KLR, to the point cloud data from UAV areal surveying to demarcate the cross-section of a river. Other than general fitting data, the cross-section of a natural river generally contains sudden variation, an angled shape, and even bumps as well as a linear shape. To accommodate all of those features of natural and manmade cross-sections, a highly flexible fitting model is requested. Furthermore, the observed data point from a UAV surveying is large enough for the point cloud dataset. Therefore, the KLR model can be chosen to fit the point cloud data for cross-sections. Different river shapes with simulation study and the experimental site study of the REC were made as well as two case studies of the Migok-cheon stream, Hapcheon-gun and the Pori-cheon stream, Yecheon-gun. From the extensive applications of the proposed model in the current study, the results conclude that the suggested KLR model can reproduce the critical characteristics of the different shape cross-sections of a river with the point cloud data from UAV aerial surveying.

The major limitation of the point cloud data employed in the current study is that RGB photographs were employed and the vegetation inside the river could generate an obscure cross-sectional shape. Further optical instruments, such as hyperspectral and lidar sensors, could be tested to overcome this limitation. However, a perfect solution that can remove the vegetation inside rivers has not yet been developed. To avoid this issue, points of the cross-section where

https://doi.org/10.5194/gmd-2023-57
Preprint. Discussion started: 27 June 2023

Geoscientific Model Development Discussions
Open Access
EGU

little vegetation exists can be selected. Also, a general UAV sensor cannot penetrate water body and a special sensor (e.g. bathymetry LiDAR) must be employed to capture the shape of the cross-section below water surface. Therefore, special care must be taken to apply the current model to UAV surveying data. The current demarcation method for a cross-section must be applied to a dry stream or very shallow stream whose flow does not affect the discharge amount. Otherwise, a bathymetry data must be employed for demarcating a cross-section of a river. Since the sensors that can penetrate water body and UAV technologies are developing fast, the proposed KLR model with the UAV surveying might become more suitable in near future to demarcate a cross-section.

The proposed KLR method can be easily adopted for other demarcation cases, such as buildings and structures. The proposed KLR method is a rather simple and direct approach for demarcating an area and structures. Additionally, other nonparametric techniques, such as LOWESS, can be further tested with extensive testing and adjustment. The current study focused on the KLR model, since the clustered data setting is obvious and easy to apply.

9. Code and data availability

The program was developed with Matlab program. All the employed code and excel files are available at Mendeley Data in <http://dx.doi.org/10.17632/xdw4cgnvhm.1>.

Competing interests

The author declares that they have no conflict of interest.

Author Contribution

T.L. carried out the research plan and programming as well as supervising while J.P. and S.H performed collection data and data curation. VS performed editing this manuscript and additional simulation studies.

Acknowledgments

The authors thank the River Experiment Center of Korea Institute of Civil Engineering and Building Technology (KICT) to open its site for measuring the experimental rivers and its cooperation.

https://doi.org/10.5194/gmd-2023-57
Preprint. Discussion started: 27 June 2023

References

Ahmad, M. I., Sinclair, C. D., and Werritty, A.: Log-logistic flood frequency analysis, Journal of Hydrology, 98, 205-224, 1988.

Allouis, T., Bailly, J., Pastol, Y., and Le Roux, C.: Comparison of LiDAR waveform processing methods for very shallow water bathymetry using Raman, near-infrared and green signals, Earth Surface Processes and Landforms, 35, 640-650, 2010.

Anders, N., Smith, M., Suomalainen, J., Cammeraat, E., Valente, J., and Keesstra, S.: Impact of flight altitude and cover orientation on Digital Surface Model (DSM) accuracy for flood damage assessment in Murcia (Spain) using a fixed-wing UAV, Earth Science Informatics, 13, 391-404, 2020.

Andreadakis, E., Diakakis, M., Vassilakis, E., Deligiannakis, G., Antoniadis, A., Andriopoulos, P., Spyrou, N. I., and Nikolopoulos, E. I.: Unmanned aerial systems-aided post-flood peak discharge estimation in ephemeral streams, Remote Sensing, 12, 1-27, 2020.

BRTMA: Reports of Fundamental River Plan for Hwanggang Downstream Rivers (http://www.river.go.kr/WebForm/sub_04/sub_04_01_01.aspx?wNM=01&subTree=2&subPeriod=999&subGrade=9&searRNM=%eb%af%b8%ea%b3%a1%ec%b2%9c&selSort=99). Agency, T. B. R. T. M. (Ed.), Ministry of Land, Infrastructure and Transport, Busan, 2019.

Chow, V. T.: Open Channel Hydraulics. , McGraw-Hill, New York, 1959.

Cleveland, W. S.: Robust locally weighted regression and smoothing scatterplots, Journal of the American Statistical Association, 74, 829-836, 1979.

Elek, P. and Márkus, L.: A long range dependent model with nonlinear innovations for simulating daily river flows, Natural Hazards and Earth System Science, 4, 277-283, 2004.

Fernandez-Diaz, J. C., Glennie, C. L., Carter, W. E., Shrestha, R. L., Sartori, M. P., Singhania, A., Legleiter, C. J., and Overstreet, B. T.: Early results of simultaneous terrain and shallow water bathymetry mapping using a single-wavelength airborne LiDAR sensor, IEEE Journal of Selected Topics in Applied Earth Observations and Remote Sensing, 7, 623-635, 2014.

Gichamo, T. Z., Popescu, I., Jonoski, A., and Solomatine, D.: River cross-section extraction from the ASTER global DEM for flood modeling, Environmental Modelling and Software, 31, 37-46, 2012.

Gracchi, T., Rossi, G., Stefanelli, C. T., Tanteri, L., Pozzani, R., and Moretti, S.: Tracking the evolution of riverbed morphology on the basis of uav photogrammetry, Remote Sensing, 13, 1-16, 2021.

https://doi.org/10.5194/gmd-2023-57
Preprint. Discussion started: 27 June 2023

Hamdi, D. A., Iqbal, F., Alam, S., Kazim, A., and MacDermott, A.: Drone forensics: A case study on DJI phantom 4, 2019.

Hugenholtz, C. H., Whitehead, K., Brown, O. W., Barchyn, T. E., Moorman, B. J., LeClair, A., Riddell, K., and Hamilton, T.: Geomorphological mapping with a small unmanned aircraft system (sUAS): Feature detection and accuracy assessment of a photogrammetrically-derived digital terrain model, Geomorphology, 194, 16-24, 2013.

Izumida, A., Uchiyama, S., and Sugai, T.: Application of UAV-SfM photogrammetry and aerial lidar to a disastrous flood: Repeated topographic measurement of a newly formed crevasse splay of the Kinu River, central Japan, Natural Hazards and Earth System Sciences, 17, 1505-1519, 2017.

Javernick, L., Brasington, J., and Caruso, B.: Modeling the topography of shallow braided rivers using Structure-from-Motion photogrammetry, Geomorphology, 213, 166-182, 2014.

Kaewwilai, A. J.: Analysis of Flood Patterns in Adams County, Pennsylvania Utilizing Drone Technology and Computer Simulations Analysis of Flood Patterns in Adams County, Pennsylvania Utilizing Drone, 57, 1-20, 2019.

Lall, U. and Sharma, A.: A nearest neighbor bootstrap for resampling hydrologic time series, Water Resources Research, 32, 679-693, 1996.

Langhammer, J.: UAV monitoring of stream restorations, Hydrology, 6, 2019.

Lee, C., Kim, J., Kang, W., Ji, W., and Jung, S.: KICT River Experiment Center, Water and Future, 55, 91-97, 2022.

Lee, G., Choi, M., Yu, W., and Jung, K.: Creation of river terrain data using region growing method based on point cloud data from UAV photography, Quaternary International, 519, 255-262, 2019.

Lee, T. and Ouarda, T. B. M. J.: Identification of model order and number of neighbors for k-nearest neighbor resampling, Journal of Hydrology, 404, 136-145, 2011.

Lee, T., Ouarda, T. B. M. J., and Yoon, S.: KNN-based local linear regression for the analysis and simulation of low flow extremes under climatic influence, Climate Dynamics, 49, 3493-3511, 2017.

Lee, T., Salas, J. D., and Prairie, J.: An Enhanced Nonparametric Streamflow Disaggregation Model with Genetic Algorithm, Water Resources Research, 46, W08545, 2010.

Lin, C., Chen, S. Y., Chen, C. C., and Tai, C. H.: Detecting newly grown tree leaves from unmanned-aerial-vehicle images using hyperspectral target detection techniques, ISPRS Journal of Photogrammetry and Remote Sensing, 142, 174-189, 2018.

https://doi.org/10.5194/gmd-2023-57
Preprint. Discussion started: 27 June 2023

Marfai, M. A., Sunarto, Khakim, N., Fatchurohman, H., Cahyadi, A., Wibowo, Y. A., and Rosaji, F. S. C.: Tsunami hazard mapping and loss estimation using geographic information system in Drini Beach, Gunungkidul Coastal Area, Yogyakarta, Indonesia, 2019.

Marteau, B., Vericat, D., Gibbins, C., Batalla, R. J., and Green, D. R.: Application of Structure-from-Motion photogrammetry to river restoration, Earth Surface Processes and Landforms, 42, 503-515, 2017.

Neal, J. C., Odoni, N. A., Trigg, M. A., Freer, J. E., Garcia-Pintado, J., Mason, D. C., Wood, M., and Bates, P. D.: Efficient incorporation of channel cross-section geometry uncertainty into regional and global scale flood inundation models, Journal of Hydrology, 529, 169-183, 2015.

Orlowsky, B., Bothe, O., Fraedrich, K., Gerstengarbe, F. W., and Zhu, X.: Future climates from bias-bootstrapped weather analogs: An application to the Yangtze River basin, Journal of Climate, 23, 3509-3524, 2010.

Perks, M. T., Russell, A. J., and Large, A. R. G.: Technical note: Advances in flash flood monitoring using unmanned aerial vehicles (UAVs), Hydrology and Earth System Sciences, 20, 4005-4015, 2016.

Petikas, I., Keramaris, E., and Kanakoudis, V.: Calculation of multiple critical depths in open channels using an adaptive cubic polynomials algorithm, Water (Switzerland), 12, 2020a.

Petikas, I., Keramaris, E., and Kanakoudis, V.: A novel method for the automatic extraction of quality non-planar river cross-sections from digital elevation models, Water (Switzerland), 12, 2020b.

Pilotti, M.: Extraction of cross sections from digital elevation model for one-dimensional dam-break wave propagation in mountain valleys, Water Resources Research, 52, 52-68, 2016.

Remondino, F., Barazzetti, L., Nex, F., Scaioni, M., and Sarazzi, D.: UAV photogrammetry for mapping and 3d modeling - Current status and future perspectives, 2011, 25-31.

Sanhueza, D., Picco, L., Ruiz-Villanueva, V., Iroumé, A., Ulloa, H., and Barrientos, G.: Quantification of fluvial wood using UAVs and structure from motion, Geomorphology, 345, 2019.

Seong, K., Lee, S. O., Jung, H. J., and Lee, T.: Safety first? Lessons from the Hapcheon Dam flood in 2020, Natural Hazards, In Review, 2020.

Siebert, S. and Teizer, J.: Mobile 3D mapping for surveying earthwork projects using an Unmanned Aerial Vehicle (UAV) system, Automation in Construction, 41, 1-14, 2014.

Simonoff, J. S.: Smoothing Methods in Statistics, Springer-Verlag, New York, 1996.

Smith, M. W., Carrivick, J. L., Hooke, J., and Kirkby, M. J.: Reconstructing flash flood magnitudes using 'Structure-from-Motion': A rapid assessment tool, Journal of Hydrology, 519, 1914-1927, 2014.

https://doi.org/10.5194/gmd-2023-57
Preprint. Discussion started: 27 June 2023

Geoscientific Model Development
Discussions

Srivastava, K., Pandey, P. C., and Sharma, J. K.: An approach for route optimization in applications of precision agriculture using uavs, Drones, 4, 1-24, 2020.

Taddia, Y., Pellegrinelli, A., Corbau, C., Franchi, G., Staver, L. W., Stevenson, J. C., and Nardin, W.: High-resolution monitoring of tidal systems using UAV: A case study on poplar island, MD (USA), Remote Sensing, 13, 2021.

Tomsett, C. and Leyland, J.: Remote sensing of river corridors: A review of current trends and future directions, River Research and Applications, 35, 779-803, 2019.

Wang, S., Ahmed, Z., Hashmi, M. Z., and Pengyu, W.: Cliff face rock slope stability analysis based on unmanned arial vehicle (UAV) photogrammetry, Geomechanics and Geophysics for Geo-Energy and Geo-Resources, 5, 333-344, 2019.

Watanabe, Y. and Kawahara, Y.: UAV Photogrammetry for Monitoring Changes in River Topography and Vegetation, Procedia Engineering, 154, 317-325, 2016.

Yan, Y., Ma, S., Yin, S., Hu, S., Long, Y., Xie, C., and Jiang, H.: Detection and Numerical Simulation of Potential Hazard in Oil Pipeline Areas Based on UAV Surveys, Frontiers in Earth Science, 9, 2021.

Zakaria, S., Mahadi, M. R., Abdullah, A. F., and Abdan, K.: Aerial platform reliability for flood monitoring under various weather conditions: A review, 2018, 591-602.

https://doi.org/10.5194/gmd-2023-57
Preprint. Discussion started: 27 June 2023

Geoscientific Model Development Discussions
Open Access
EGU

Table 1. Performance measures of RMSE and MAE for three different models, KLR, LOWESS, and PolyFit, for synthetically simulated data of three different shape cross-sections as trapezoidal, U-shape, and V-shape.

	Shape	KLR	LOWESS	PolyFit4
RMSE	Trapezoid	0.0289	0.1397	0.1565
	U-shape	0.0326	0.1868	0.1728
	V-shape	0.0325	0.1353	0.2299
MAE	Trapezoid	0.1549	0.3697	0.3789
	U-shape	0.1536	0.3158	0.3518
	V-shape	0.1558	0.2807	0.4369

Table 2. Performance measures of RMSE for three different models as KLR, LOWESS, and PolyFit for the river experiment center (REC).

	No	KLR	LOWESS	Polynomial		
				2	3	4
I-shape	1	**0.072**	0.125	0.183	0.183	0.138
	2	**0.101**	0.154	0.231	0.235	0.156
	3	**0.074**	0.192	0.281	0.284	0.148
	4	**0.054**	0.12	0.17	0.174	0.177
	5	**0.054**	0.17	0.33	0.291	0.289
	6	**0.062**	0.127	0.359	0.287	0.205
U-shape	1	**0.029**	0.074	0.134	0.13	0.088
	2	**0.066**	0.118	0.182	0.155	0.119
	3	**0.045**	0.072	0.113	0.111	0.094
	4	**0.054**	0.083	0.149	0.146	0.105
	5	**0.170**	0.183	0.196	0.183	0.219
	6	**0.131**	0.183	0.374	0.363	0.201
	7	**0.171**	0.246	0.419	0.427	0.204
S-shape	1	**0.122**	0.145	0.435	0.429	0.151
	2	**0.088**	0.112	0.398	0.398	0.118
	3	0.204	0.216	0.428	0.416	**0.203**
	4	**0.164**	0.197	0.452	0.467	0.178
	5	**0.187**	0.186	0.433	0.419	0.213
	6	**0.123**	0.146	0.402	0.404	0.136
	7	**0.145**	0.146	0.48	0.488	0.22

https://doi.org/10.5194/gmd-2023-57
Preprint. Discussion started: 27 June 2023

Geoscientific Model Development
Discussions
Open Access
EGU

Table 3. Performance measures of MAE for three different models as KLR, LOWESS, and PolyFit for the river experiment center (REC).

	No	KLR	LOWESS	Polynomial		
				2	3	4
I-shape	1	**0.062**	0.114	0.162	0.163	0.13
	2	**0.083**	0.135	0.194	0.197	0.125
	3	**0.06**	0.146	0.183	0.184	0.123
	4	**0.048**	0.097	0.142	0.143	0.144
	5	**0.04**	0.112	0.275	0.233	0.178
	6	**0.05**	0.098	0.299	0.224	0.139
U-shape	1	**0.021**	0.061	0.117	0.112	0.08
	2	**0.059**	0.104	0.141	0.132	0.105
	3	**0.035**	0.058	0.099	0.098	0.076
	4	**0.039**	0.072	0.126	0.126	0.091
	5	**0.117**	0.14	0.173	0.142	0.177
	6	**0.083**	0.151	0.3	0.29	0.169
	7	**0.148**	0.209	0.341	0.331	0.167
S-shape	1	**0.094**	0.113	0.377	0.339	0.12
	2	**0.082**	0.091	0.342	0.344	0.105
	3	0.167	0.173	0.36	0.33	**0.162**
	4	**0.142**	0.156	0.392	0.368	0.154
	5	**0.147**	0.136	0.379	0.374	0.19
	6	0.101	0.117	0.372	0.371	**0.1**
	7	**0.118**	0.112	0.43	0.43	0.172

Table 4. Performance measures of RMSE and MAE for three different models as KLR, LOWESS, and PolyFit for four sites of Hapcheon-gun.

	Site No.	KLR	LOWESS	PolyFit2	PolyFit3	PolyFit4
RMSE	Site-1	0.4063	0.8389	1.8548	1.8046	1.4218
	Site-2	0.4010	0.6736	1.3762	1.1252	0.8753
	Site-3	0.3236	0.4514	1.4722	1.4327	0.9753
	Site-4	0.4786	0.9419	1.3834	1.9593	0.7068
MAE	Site-1	0.5393	0.8197	1.3034	1.2934	1.1224
	Site-2	0.4406	0.5764	1.1758	1.1611	0.9482
	Site-3	0.5746	0.7439	1.1536	1.0342	0.8221
	Site-4	0.6422	0.8307	1.1500	1.1057	0.7615

https://doi.org/10.5194/gmd-2023-57
Preprint. Discussion started: 27 June 2023

Geoscientific Model Development
Discussions
Open Access

Table 5. Performance measures of MAE and RMSE for three different models as KLR, LOWESS, and PolyFit for Yecheon.

	Site No.	KLR	LOWESS	PolyFit2	PolyFit3	PolyFit4
RMSE	Y1	**0.235**	0.461	0.652	0.566	0.533
	Y2	**0.135**	0.279	0.750	0.721	0.377
	Y3	**0.092**	0.236	0.693	0.659	0.401
	Y4	**0.068**	0.116	0.425	0.362	0.124
MAE	Y1	**0.158**	0.356	0.544	0.446	0.435
	Y2	**0.098**	0.223	0.678	0.647	0.289
	Y3	**0.073**	0.178	0.634	0.571	0.353
	Y4	**0.047**	0.079	0.240	0.232	0.108

https://doi.org/10.5194/gmd-2023-57
Preprint. Discussion started: 27 June 2023

Geoscientific Model Development
Discussions
Open Access

Figure

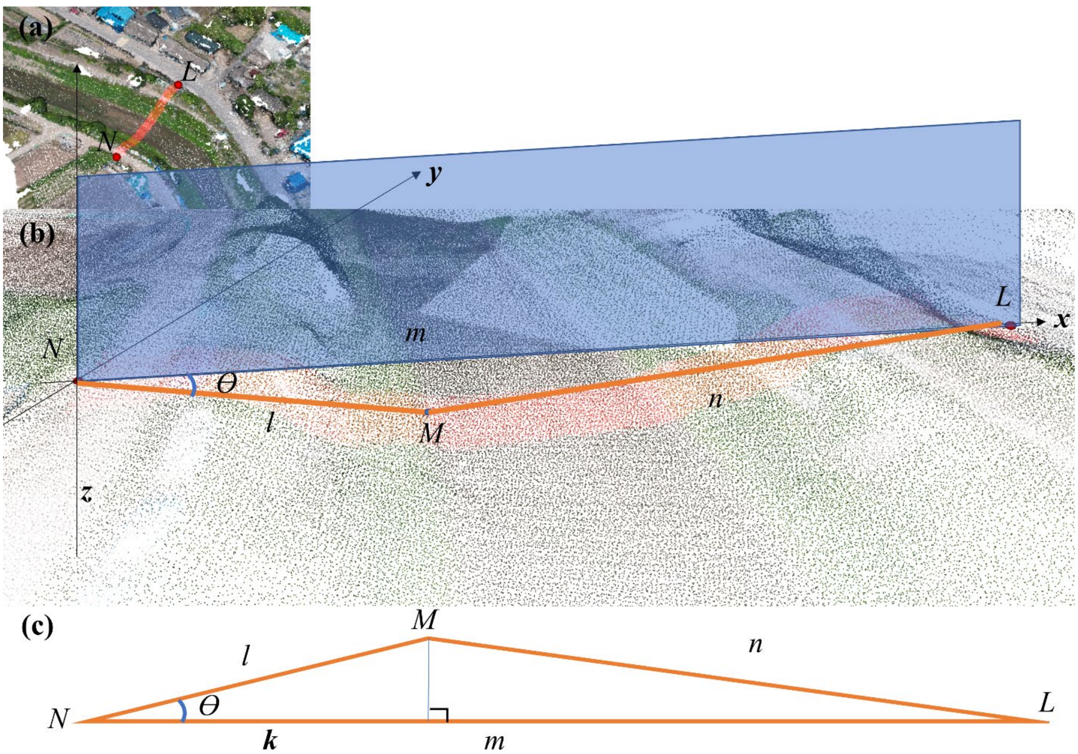

Figure 1. Example of the distance measurement: (a) aerial photo with a selected cross-section (two red dots, L and N, and thick red line); (b) magnified photo of Panel (a) with assisted 3D axis (x, y, and z) and the selected point (M); (c) emphasized triangle with the points of NML. Note that (1) the cross-section can be defined with the x-axis by connecting points N and L with the line; (2) the point M is the example point that contains the red line at Panel (a), which is a group of points in reality; and (3) the actual distance of M from N in the x-axis is represented as *k*, which can be designated as N to the point that meets line NL perpendicularly from M. The aerial images were taken from the authors.

https://doi.org/10.5194/gmd-2023-57
Preprint. Discussion started: 27 June 2023

Geoscientific Model Development
Discussions
Open Access

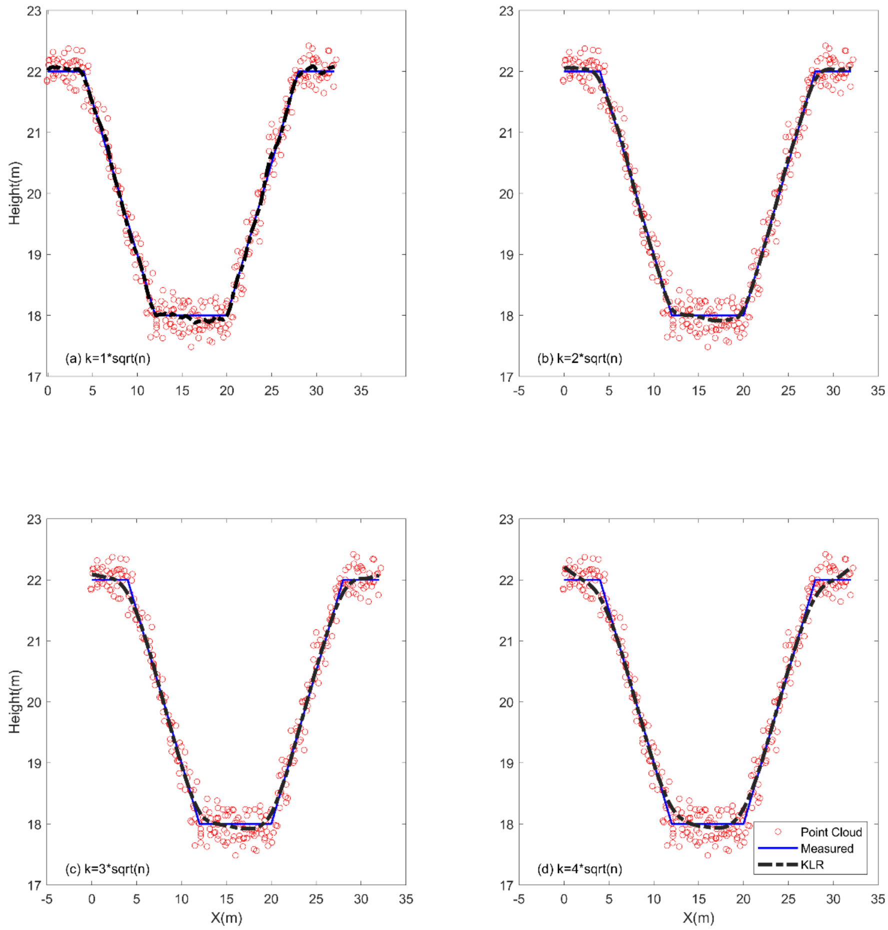

Figure 2. Assumed synthetic trapezoidal channel (not a real one) to test the KLR model (thick black dotted line) for the point cloud data with different portions of the number of neighbors ($k = a\sqrt{n}$, here a=1, 2, 3, and 4 at each panel). Note that (1) the trapezoidal sections are consistent with a 4 m top both sides and a 6 m base width as well as a 1:1 side slope with a 6 m height; (2) the number of points for the channel was divided at each 0.1 m to a total of 161 points (blue line); (3) 2 times the divided data are simulated with Eq.(17) to a total of 322 points (red dots); and (4) the elevation of the bottom channel was assumed to be 18 m.

https://doi.org/10.5194/gmd-2023-57
Preprint. Discussion started: 27 June 2023

Geoscientific Model Development
Discussions
Open Access

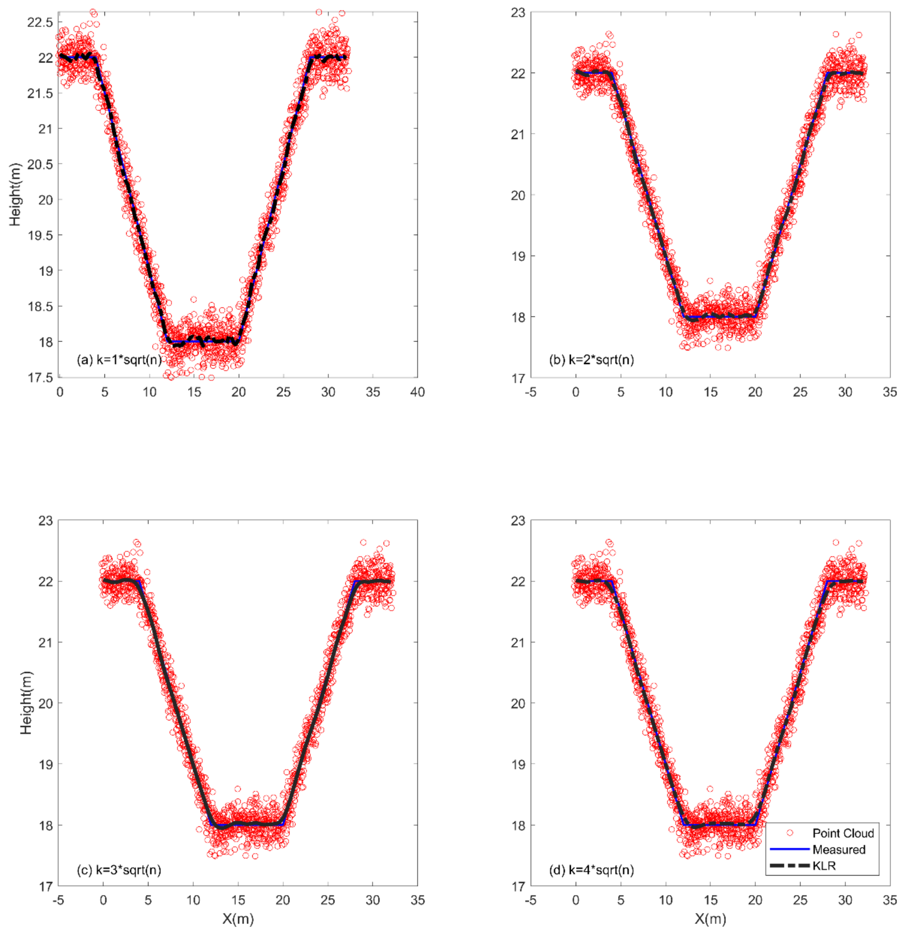

Figure 3. Assumed synthetic trapezoidal channel to test the KLR model for point cloud data with different multipliers of the number of neighbors ($k = a\sqrt{n}$). Note that (1) the trapezoidal sections are consistent with a 4 m top both sides and a 6 m base width as well as a 1:1 side slope with a 6 m height; (2) the number of points for the channel was divided at each 0.1 m to a total 161 points (blue line); (3) 10 times the divided data are simulated with Eq.(17), to a total of 1610 points (red dots) and it is 5 times more simulated cloud points than the ones in Figure 2. The difference between the number of points in the current and the one in Figure 2 was intentionally designed to illustrate how the proposed KLR model performs when there is a small number of cloud points or a large number of cloud points; and (4) the elevation of the bottom channel was assumed to be 18 m.

https://doi.org/10.5194/gmd-2023-57
Preprint. Discussion started: 27 June 2023

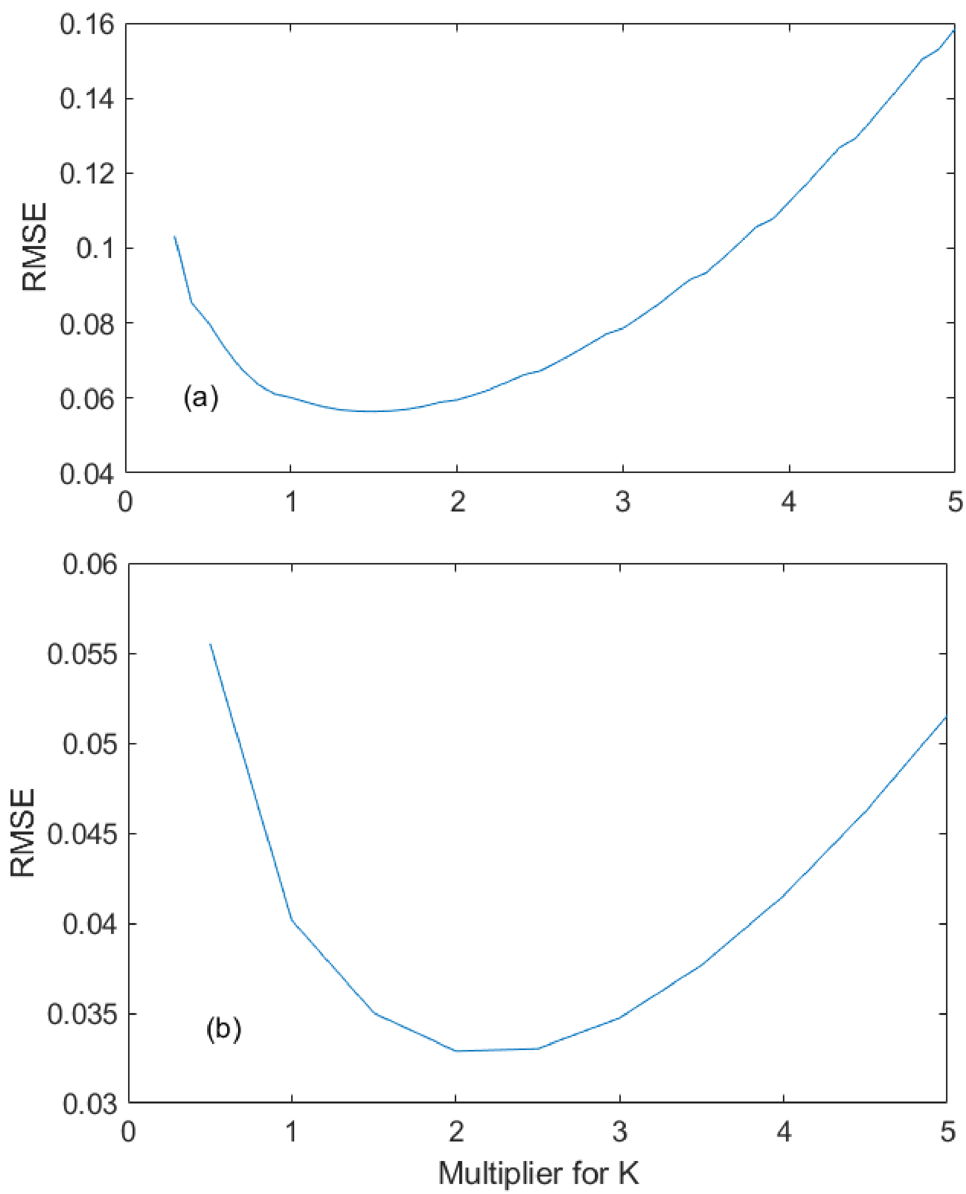

Figure 4. Root mean square error (RMSE) between the KLR estimate with different multipliers (a) of the number of neighbors ($k = a\sqrt{n}$) and the original trapezoid points for the case of 2 times the original points (panel (a)) and 10 times (panel (b)).

https://doi.org/10.5194/gmd-2023-57
Preprint. Discussion started: 27 June 2023

Geoscientific Model Development
Discussions

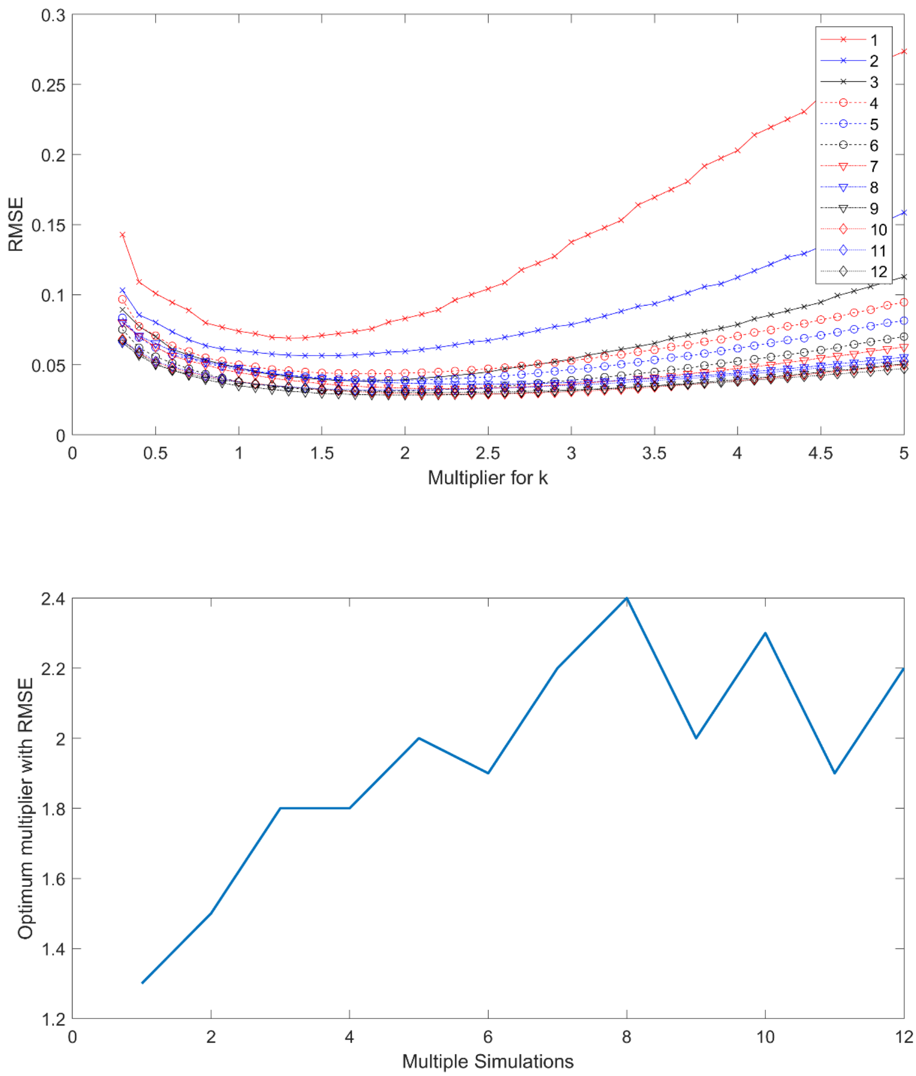

Figure 5. Root mean square error (RMSE) between the KLR estimate with different multipliers of for number of neighbors ($k = a\sqrt{n}$) and the original trapezoid points for all of the cases between 1 and 12 times the original points (top panel) as well as the optimum multiplier with the RMSE value at the top panel for each multiple simulation. Note that increasing the number of multiple simulations indicates that the number of overlapped photos is increased and the cloud points are multiplied.

https://doi.org/10.5194/gmd-2023-57
Preprint. Discussion started: 27 June 2023

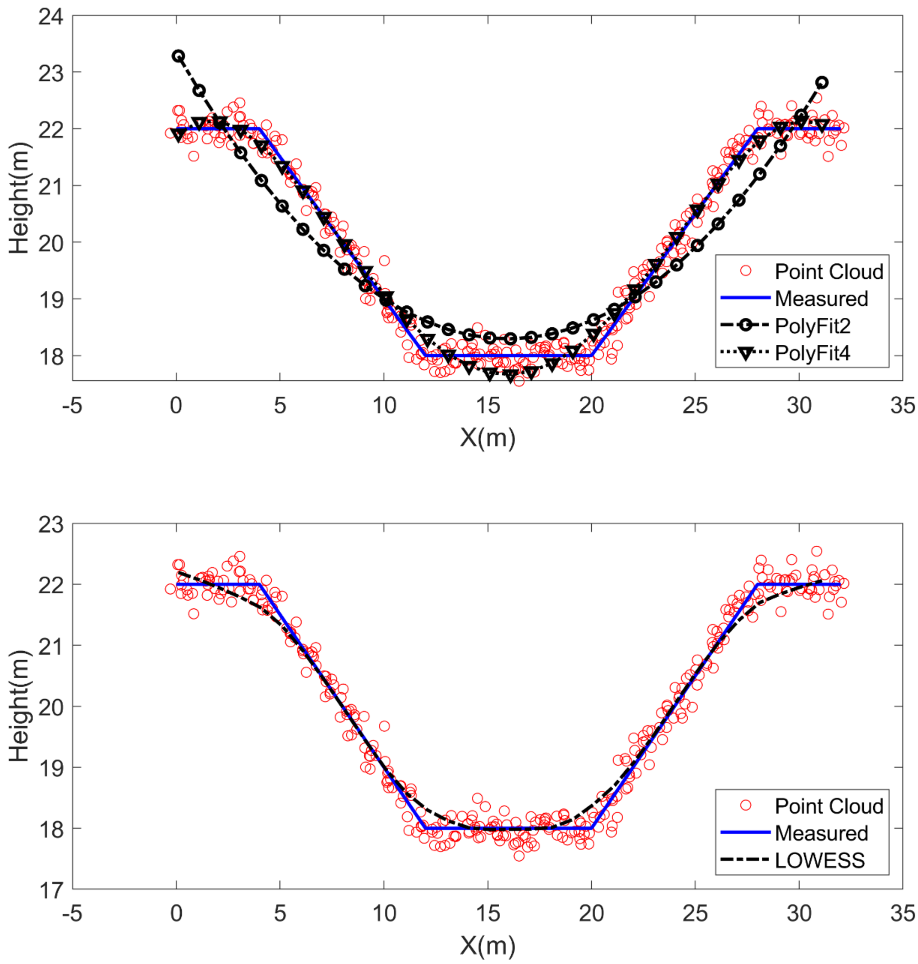

Figure 6. Polynomial regression (top panel) with the black dashed line with circles and the black dotted line with triangle markers for PolyFit2 and PolyFit4, respectively (see Eqs.(2) and (4)) and LOWESS (bottom panel, dash-dotted line) were fitted to the stochastically simulated point cloud data (red circles) of 2 times the divided points (322 points) of the synthetic trapezoidal channel points (blue line).

Geoscientific Model Development Discussions
Open Access
EGU

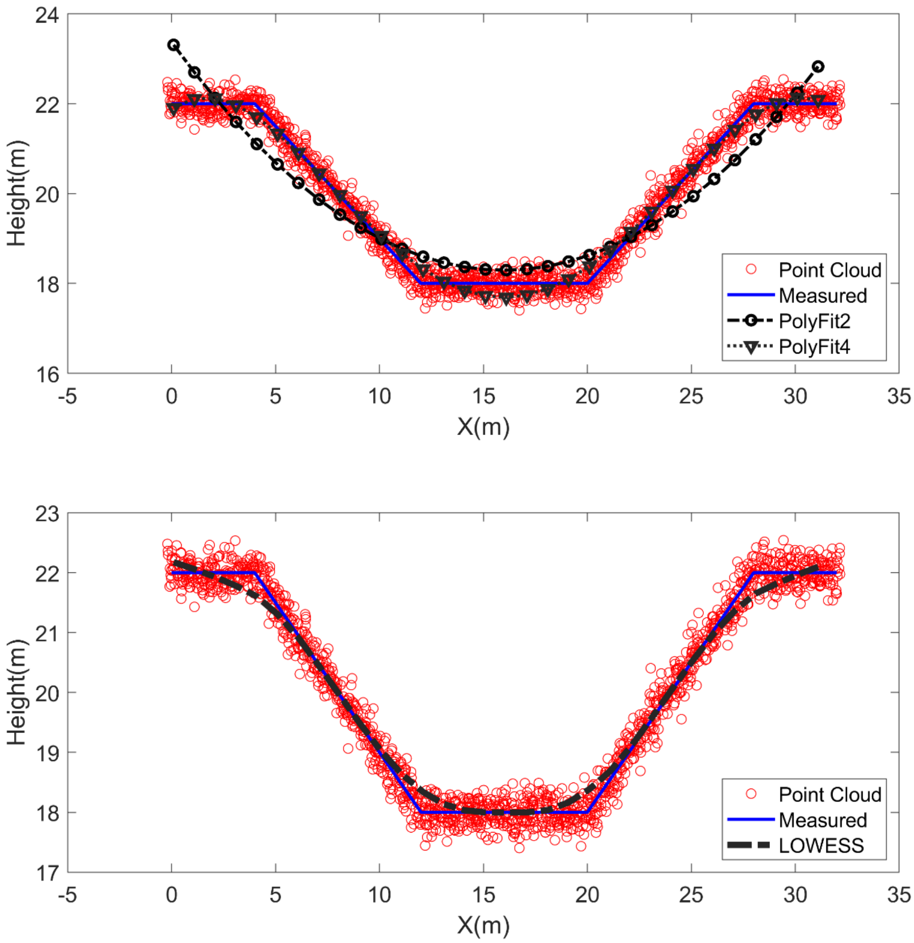

Figure 7. Polynomial regression (top panel) with the black dashed line with circles and the black dotted line with triangle markers for PolyFit2 and PolyFit4, respectively (see Eqs. (2) and (4)) and LOWESS (the dash-dotted line in the bottom panel) fitted to the simulated point cloud data (red circles) of 10 times the synthetic trapezoidal channel points (blue line) with Eq.(17).

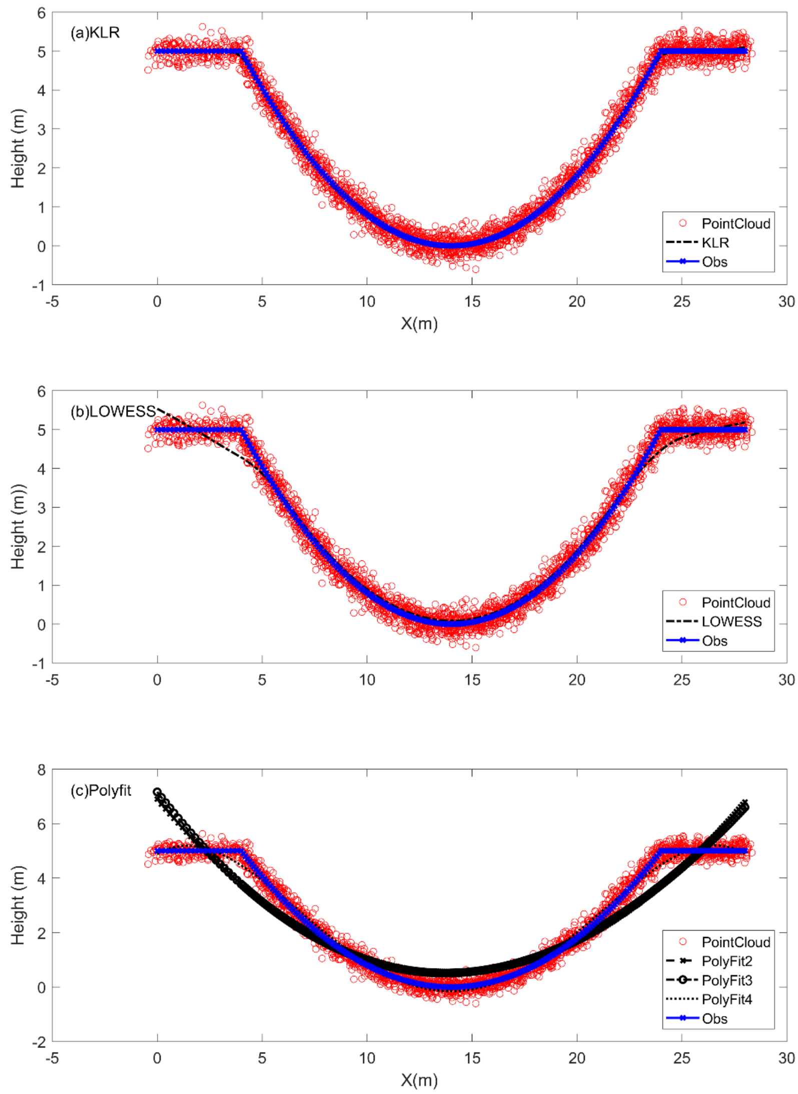

Figure 8. Synthetic U-shape river cross-section (blue solid line with cross markers) and the simulated point could data (red circles) of 10 times the synthetic channel (2620 points total) with Eq.(17) as well as the fitted estimates to KLR (the panel(a)), LOWESS (the panel(b)), and PolyFit (the panel(c)). Note that the U-shape river cross-section was designed with the power function as in Eqs. (19) and (20) and the U-shape was synthetically built following the reference of Neal et al. (2015) and the section was divided into 262 points.

https://doi.org/10.5194/gmd-2023-57
Preprint. Discussion started: 27 June 2023

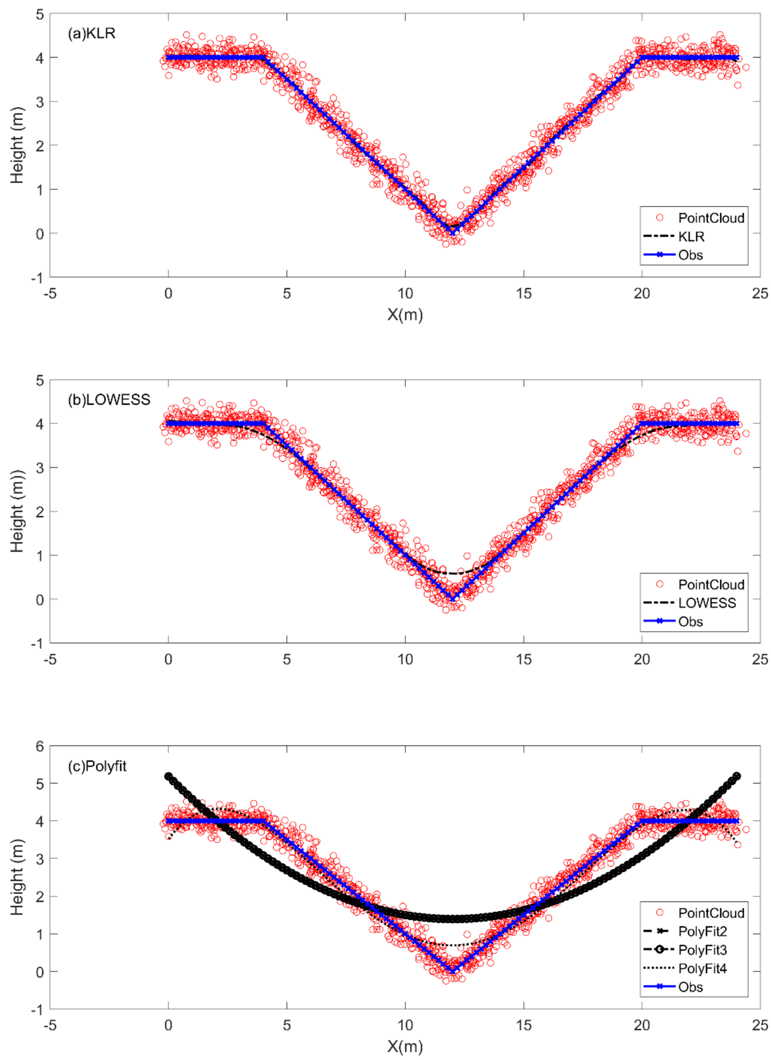

Figure 9. Synthetic V-shape river cross-section (blue solid line with cross markers) and the simulated point could data (red circles) of 10 times the synthetic channel (2620 points total) with Eq.(17) as well as the fitted estimates to KLR (the panel(a)), LOWESS (the panel(b)), and PolyFit (the panel(c)). Note that (1) the V-shape river cross-section was designed with the height of 4 m and top width of 16 m and the section was divided into 121points.

https://doi.org/10.5194/gmd-2023-57
Preprint. Discussion started: 27 June 2023

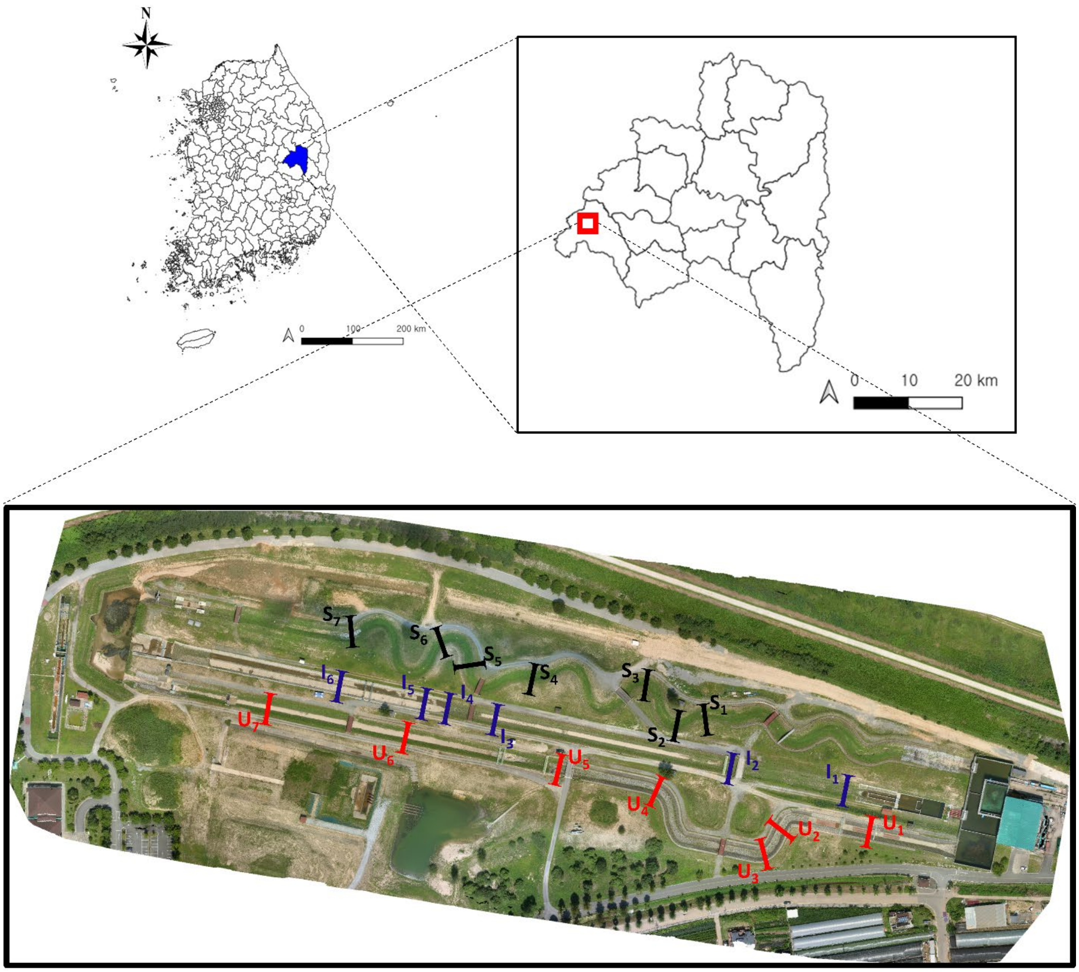

Figure 10. Location of the River Experiment Center (REC) at the top panels and the selected channels of the ground surveying for the straight river with I-shape (I_1,...I_6), the meandering river with S-shape (S_1,...,S_7), and the steep river with U-shape (U_1,...,U_7) rivers. The aerial image is taken and produced by the authors and no copyright is required.

https://doi.org/10.5194/gmd-2023-57
Preprint. Discussion started: 27 June 2023

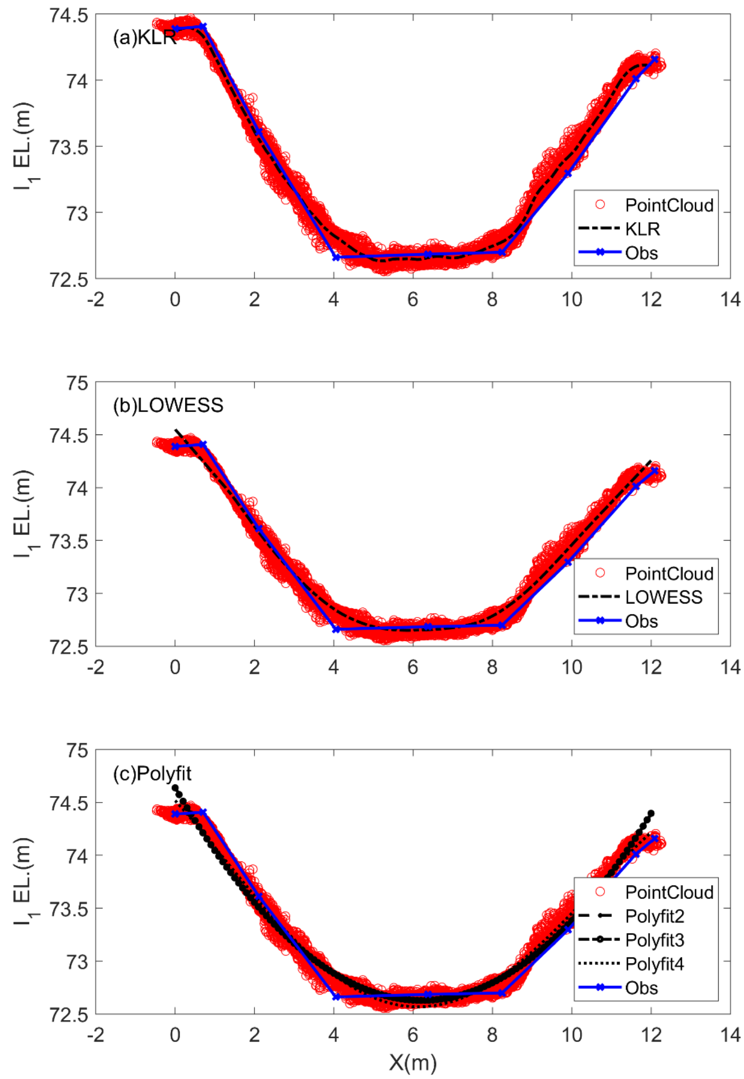

963

964 Figure 11. Point cloud data (red circles) for the channel I_1 of the REC site and model-fitted line
965 (black dashed line) with KLR (panel(a)), LOWESS (panel(b)), and PolyFit (panel(c)) as well as
966 the ground surveying.

967

https://doi.org/10.5194/gmd-2023-57
Preprint. Discussion started: 27 June 2023

Geoscientific Model Development
Discussions
Open Access

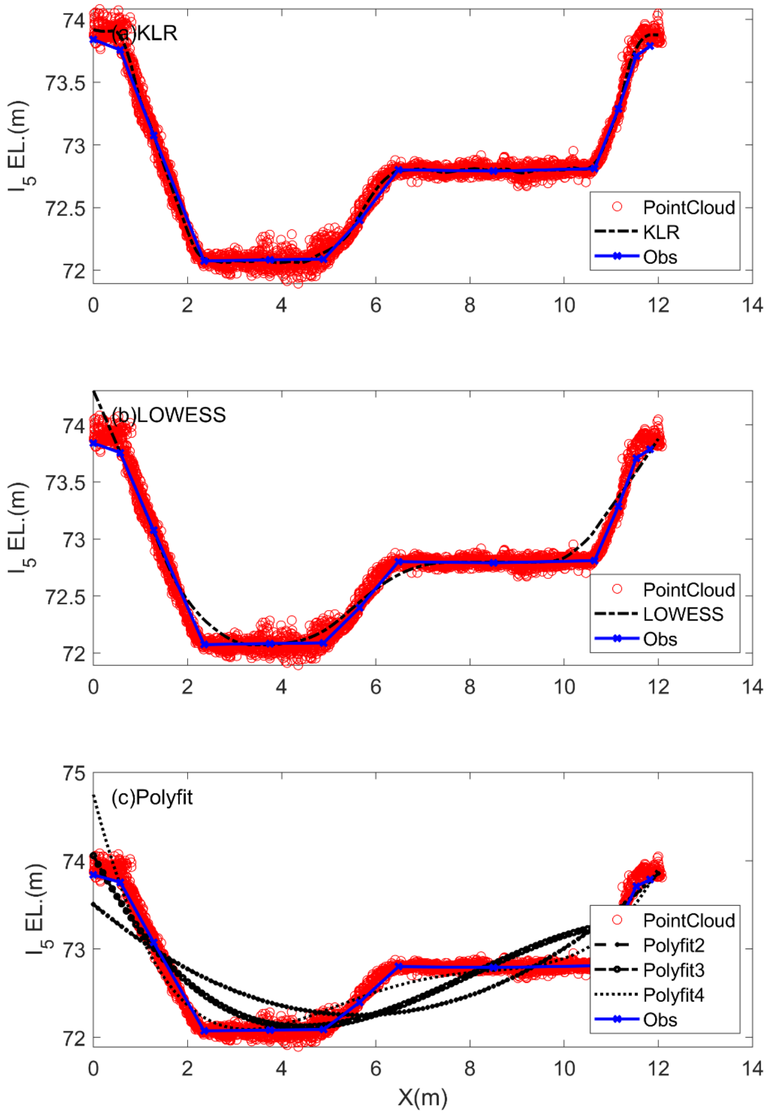

Figure 12. Point cloud data (red circles) for the channel I_5 of the REC and model-fitted line (black dashed line) with KLR (panel(a)), LOWESS (panel(b)), and PolyFit (panel(c)) as well as the ground surveying.

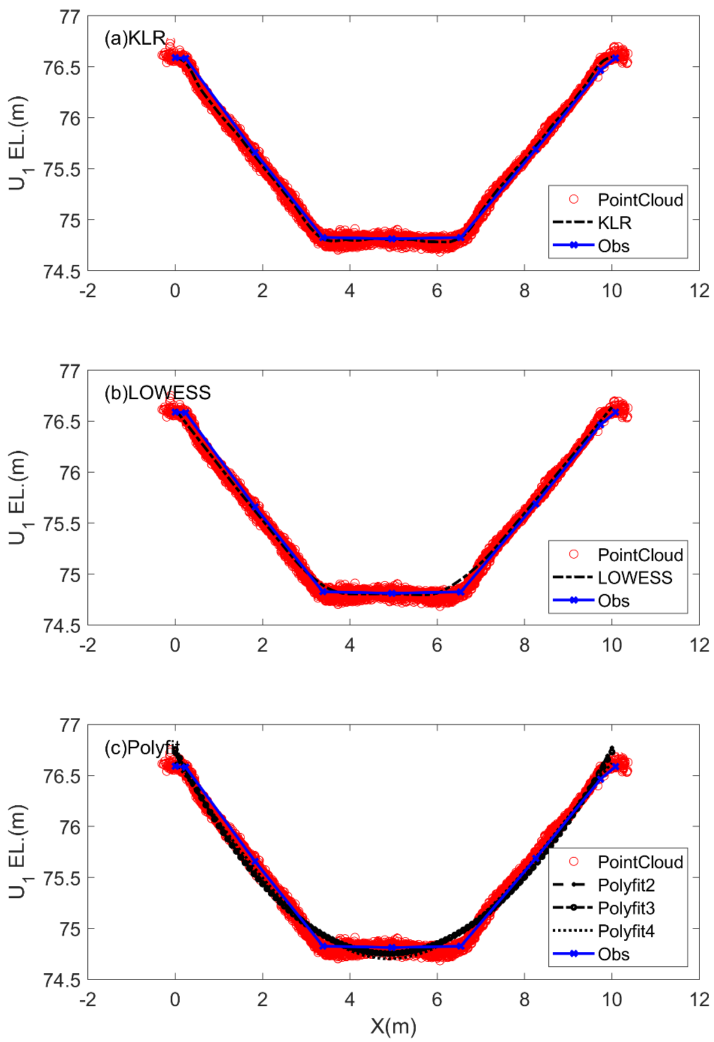

Figure 13. Point cloud data (red circles) for the channel U_1 of the REC and model-fitted line (black dashed line) with KLR (panel(a)), LOWESS (panel(b)), and PolyFit (panel(c)) as well as the ground surveying.

https://doi.org/10.5194/gmd-2023-57
Preprint. Discussion started: 27 June 2023

Geoscientific Model Development
Discussions

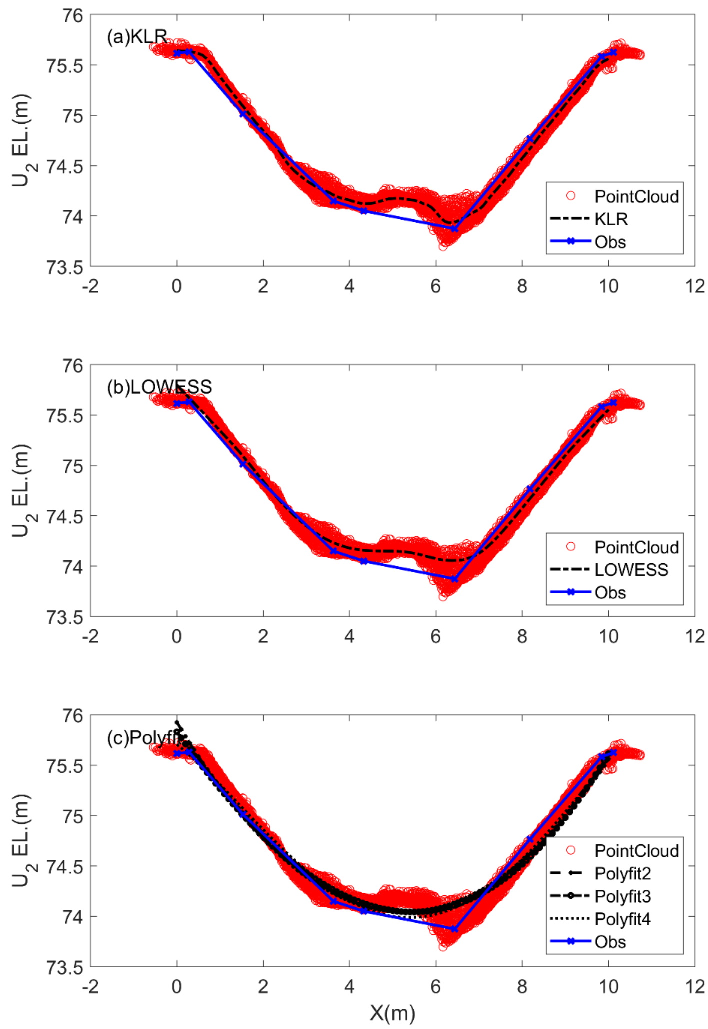

Figure 14. Point cloud data (red circles) for the channel U_2 of the REC and model-fitted line (black dashed line) with KLR (panel(a)), LOWESS (panel(b)), and PolyFit (panel(c)) as well as the ground surveying.

https://doi.org/10.5194/gmd-2023-57
Preprint. Discussion started: 27 June 2023

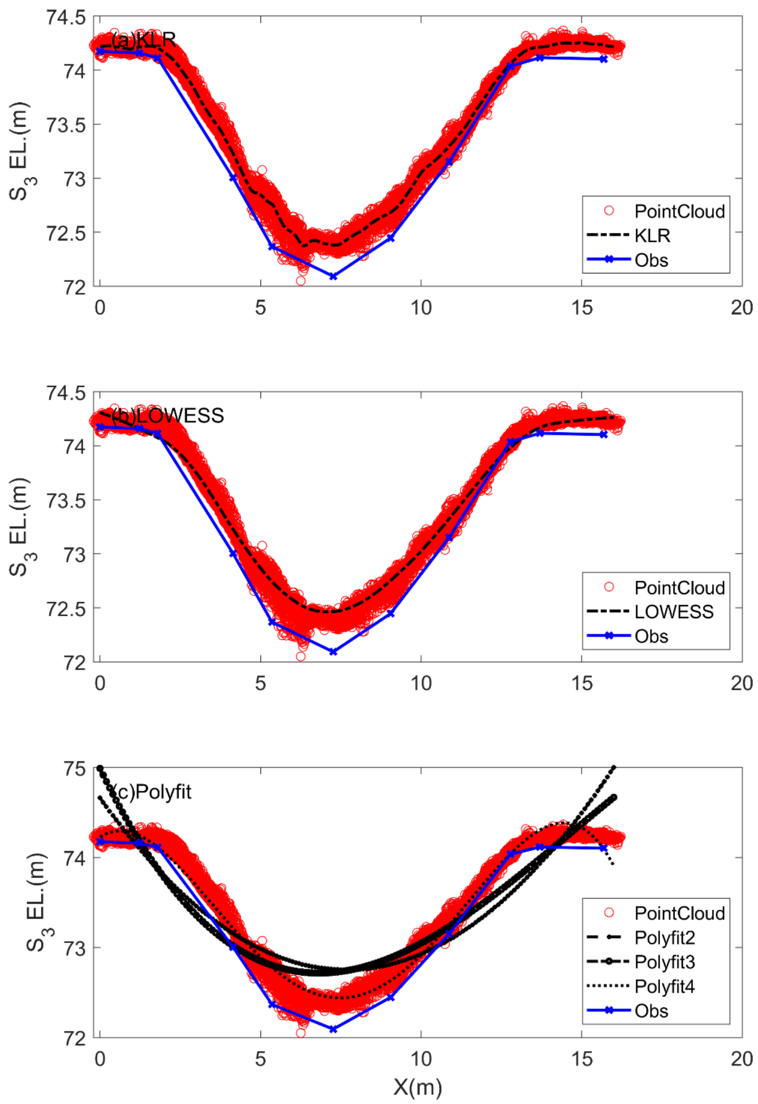

Figure 15. Point cloud data (red circles) for the channel S_3 of the REC and model-fitted line (black dashed line) with KLR (panel(a)), LOWESS (panel(b)), and PolyFit (panel(c)) as well as the ground surveying.

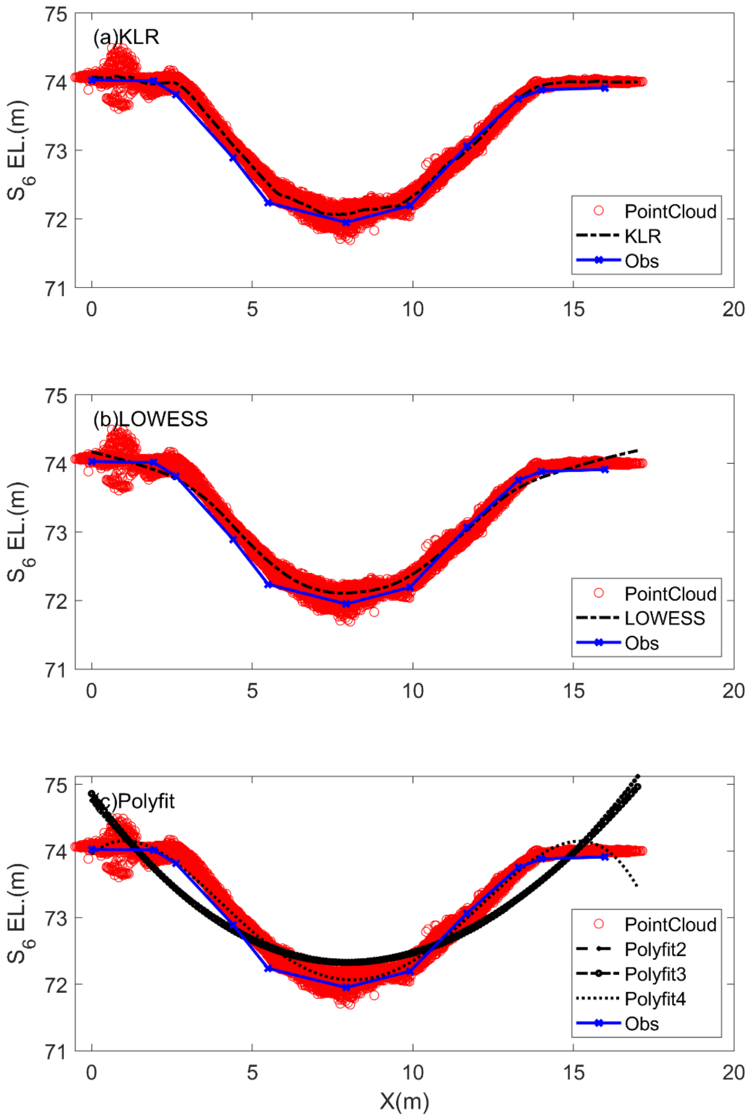

Figure 16. Point cloud data (red circles) for the channel S_6 of the REC and model-fitted line (black dashed line) with KLR (panel(a)), LOWESS (panel(b)), and PolyFit (panel(c)) as well as the ground surveying (blue solid line with x marker).

https://doi.org/10.5194/gmd-2023-57
Preprint. Discussion started: 27 June 2023

994

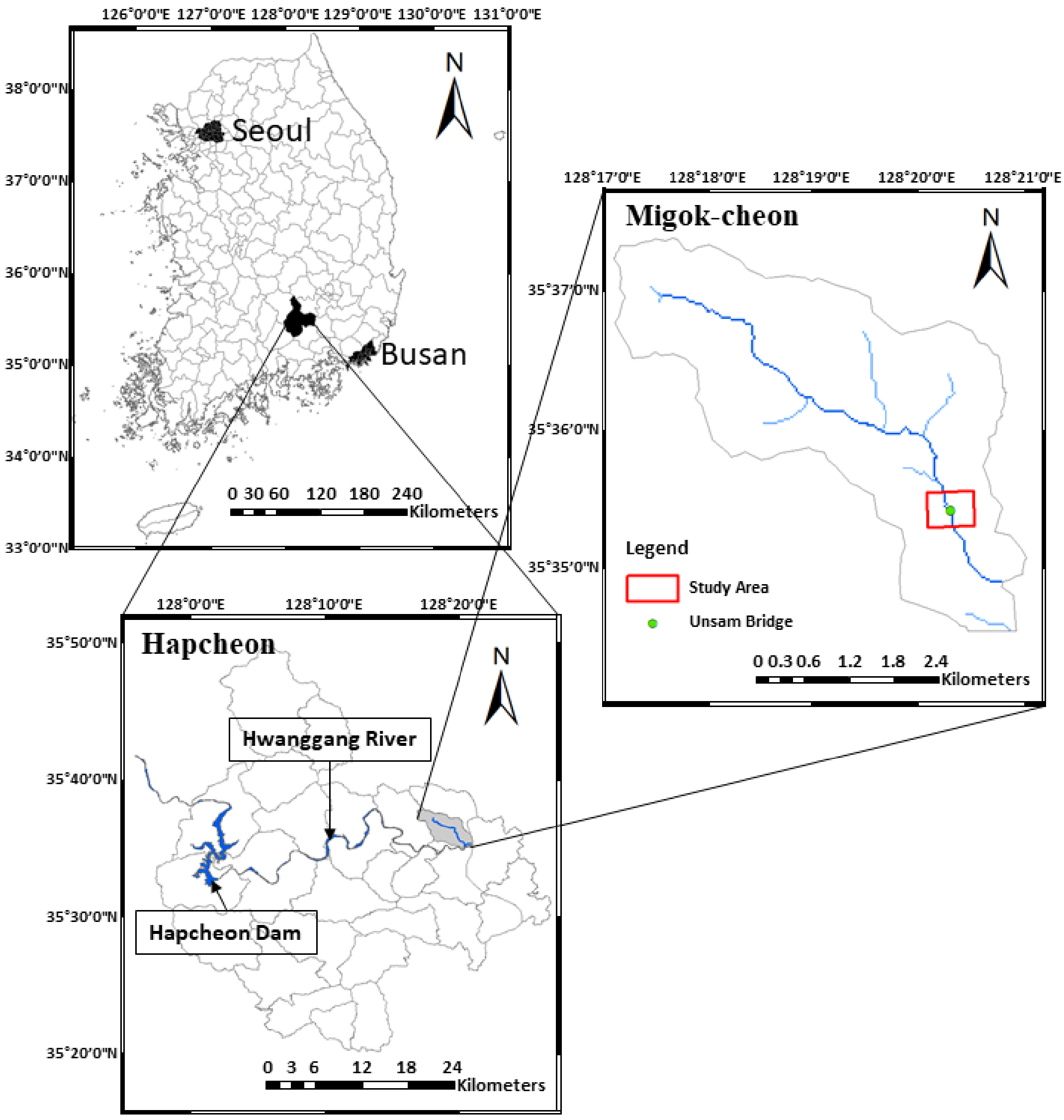

995

996 Figure 17. Study area of the applied stream, Migok-cheon in South Korea, located in the
997 province of Hapcheon-gun.

998

https://doi.org/10.5194/gmd-2023-57
Preprint. Discussion started: 27 June 2023

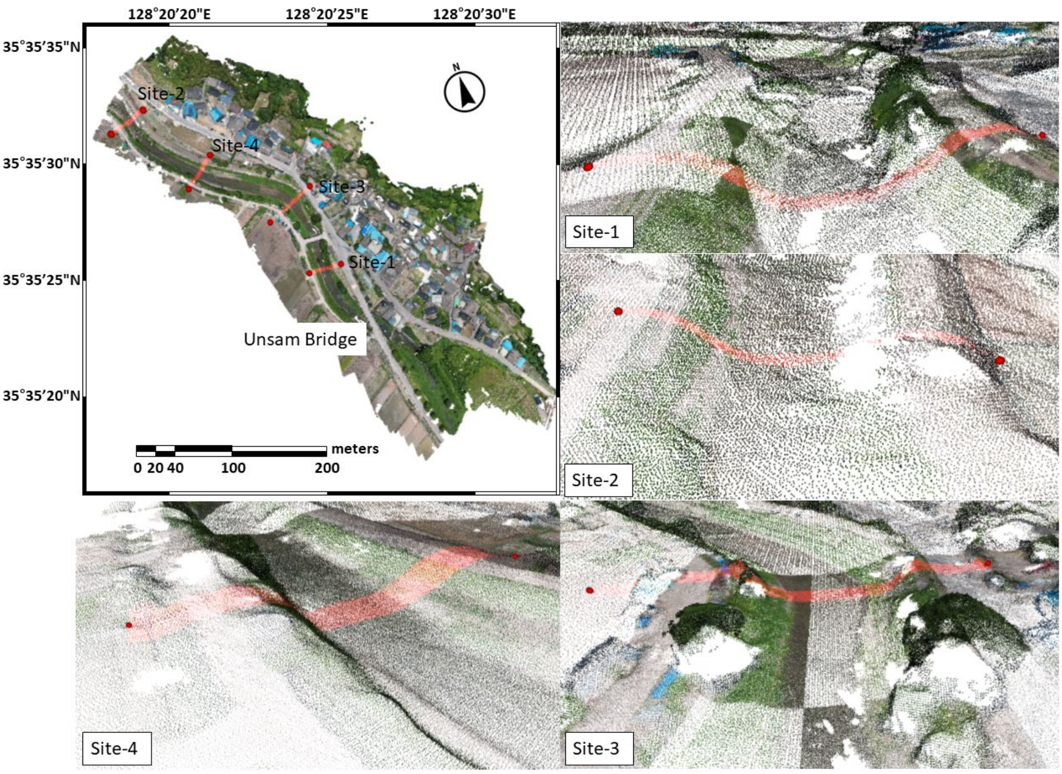

Figure 18. Locations of four tested sites in the Migok-cheon stream. Note that the other four panels surrounding the left-top panel magnify each tested site by showing the point clouds of the observed data taken from the UAV photographs. The aerial images were taken from the authors.

https://doi.org/10.5194/gmd-2023-57
Preprint. Discussion started: 27 June 2023

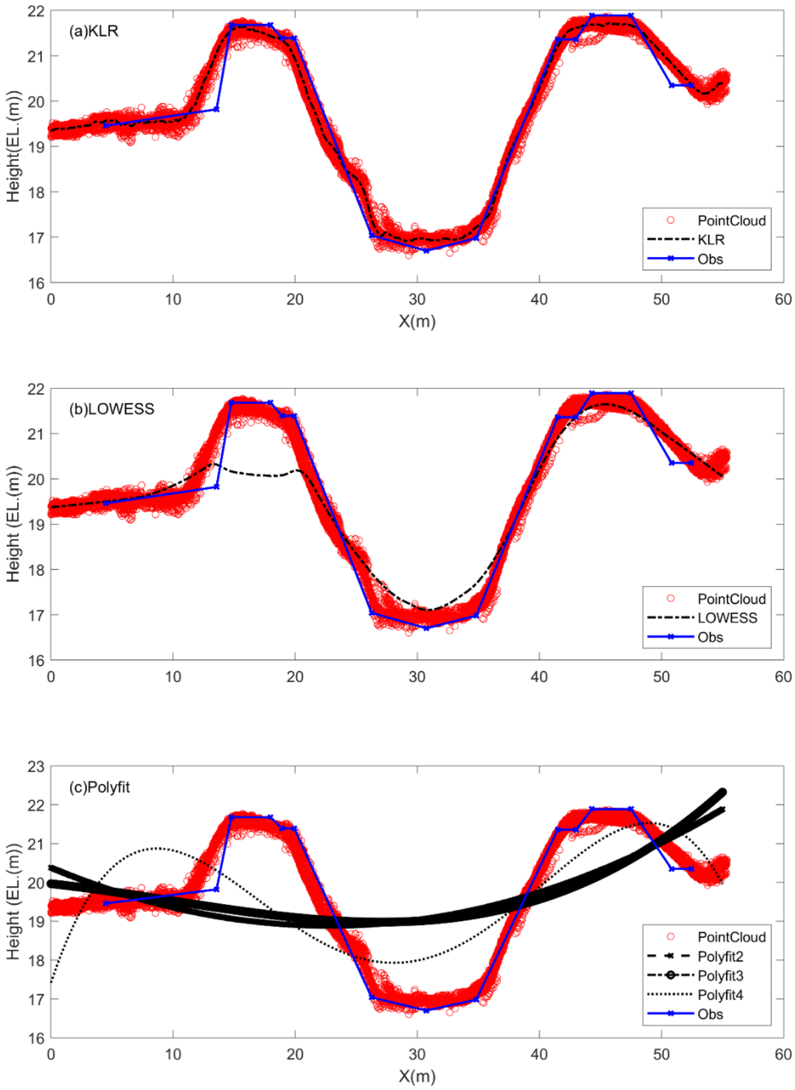

Figure 19. Point cloud data (red circles) for Site-1 and model-fitted line (black dashed line) with KLR (panel(a)), LOWESS (panel(b)), and PolyFit (panel(c)) as well as the observed surveying. Note that (1) the observed line was drawn from the previous surveying in BRTMA (2019); and (2) the detailed information including the map is attached in Supplementary Material (Figures S1 and S2 as well as Table 1).

https://doi.org/10.5194/gmd-2023-57
Preprint. Discussion started: 27 June 2023

Geoscientific Model Development
Discussions
Open Access
EGU

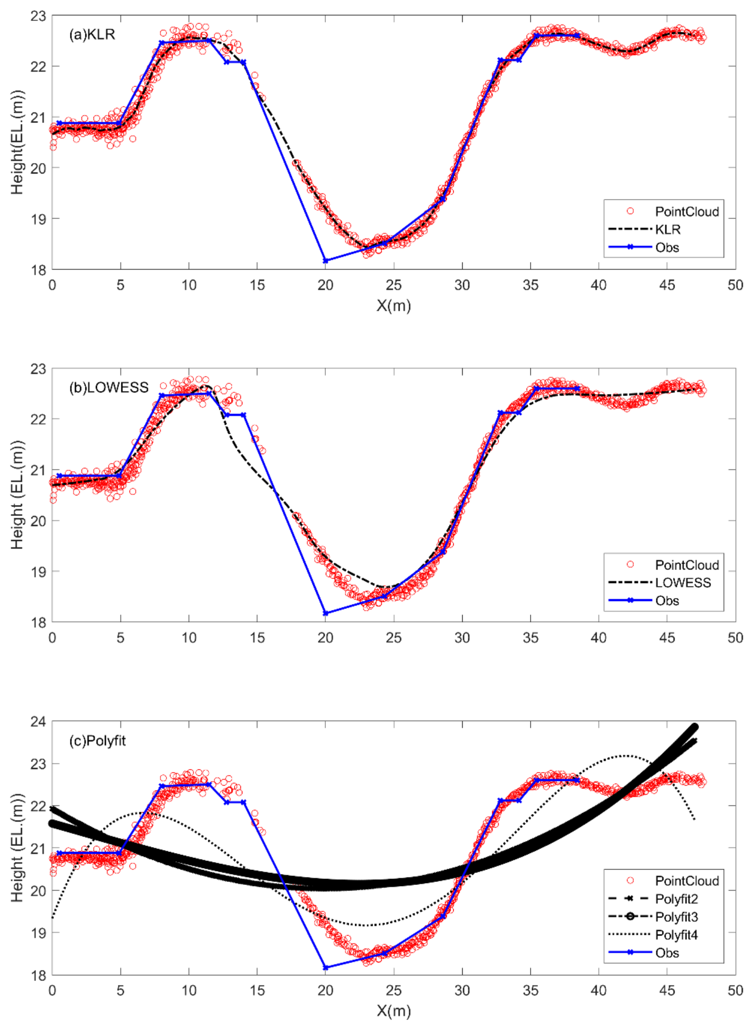

Figure 20. Point cloud data (red circles) for Site-2 and model-fitted line (black dashed line) with KLR (panel(a)), LOWESS (panel(b)), and PolyFit (panel(c)) as well as the observed surveying. Note that (1) the observed line was drawn from the previous surveying in BRTMA (2019); and (2) the detailed information including the map is attached in Supplementary Material (Figures S1 and S2 as well as Table 1).

https://doi.org/10.5194/gmd-2023-57
Preprint. Discussion started: 27 June 2023

Geoscientific Model Development
Discussions

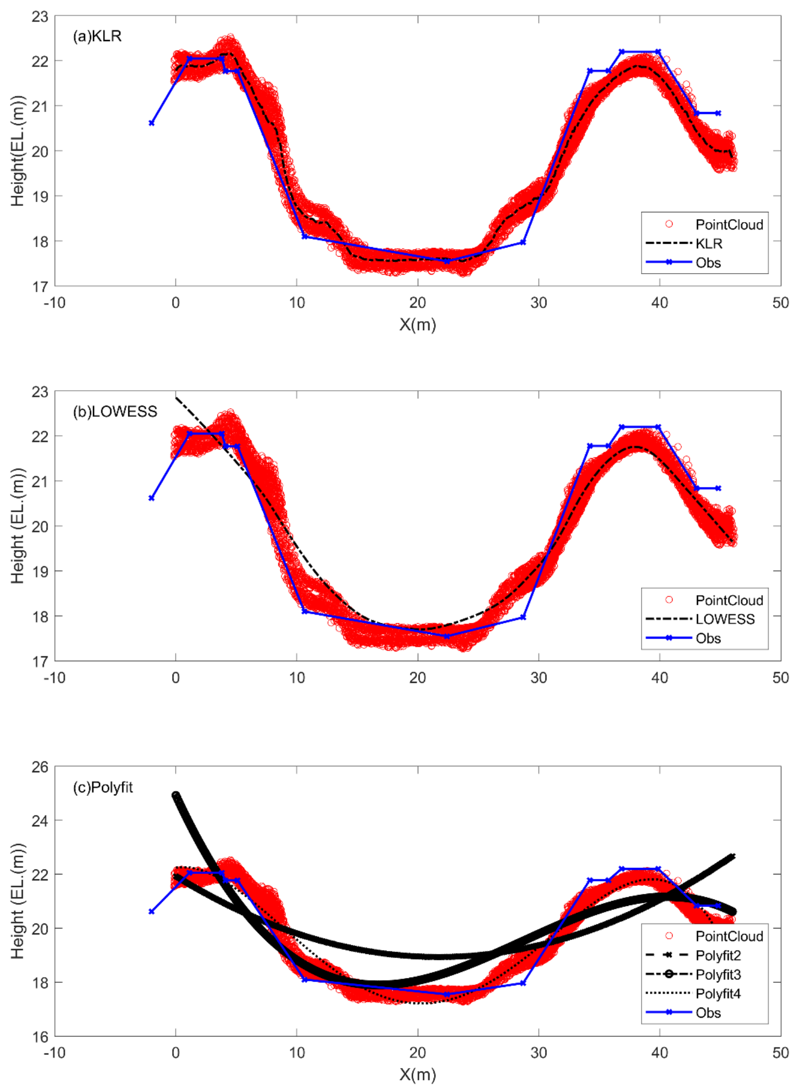

Figure 21. Point cloud data (red circles) for Site-3 and model-fitted line (black dashed line) with KLR (panel(a)), LOWESS (panel(b)), and PolyFit (panel(c)) as well as the observed surveying. Note that (1) the observed line was drawn from the previous surveying in BRTMA (2019); and (2) the detailed information including the map is attached in Supplementary Material (Figures S1 and S2 as well as Table 1).

https://doi.org/10.5194/gmd-2023-57
Preprint. Discussion started: 27 June 2023

Geoscientific Model Development
Discussions

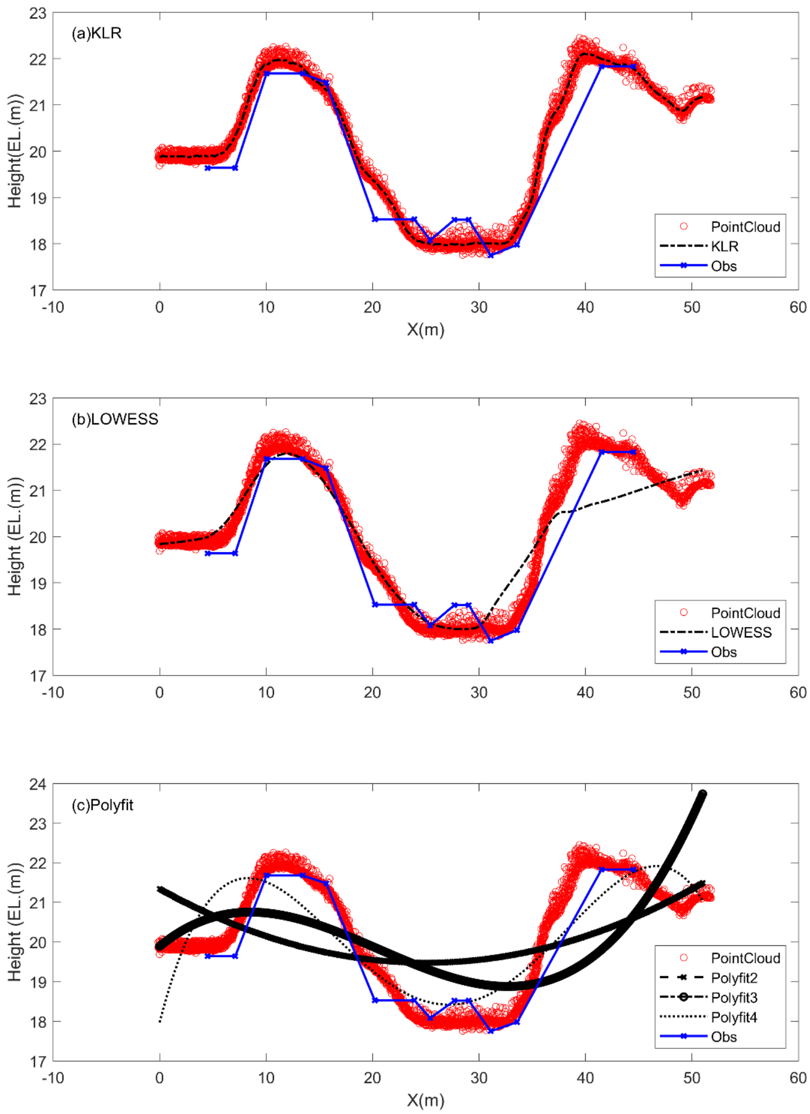

Figure 22. Point cloud data (red circles) for Site-4 and model-fitted line (black dashed line) with KLR (panel(a)), LOWESS (panel(b)), and PolyFit (panel(c)) as well as the observed surveying. Note that (1) the observed line was drawn from the previous surveying in BRTMA (2019); and (2) the detailed information including the map is attached in Supplementary Material (Figures S1 and S2 as well as Table 1).

https://doi.org/10.5194/gmd-2023-57
Preprint. Discussion started: 27 June 2023

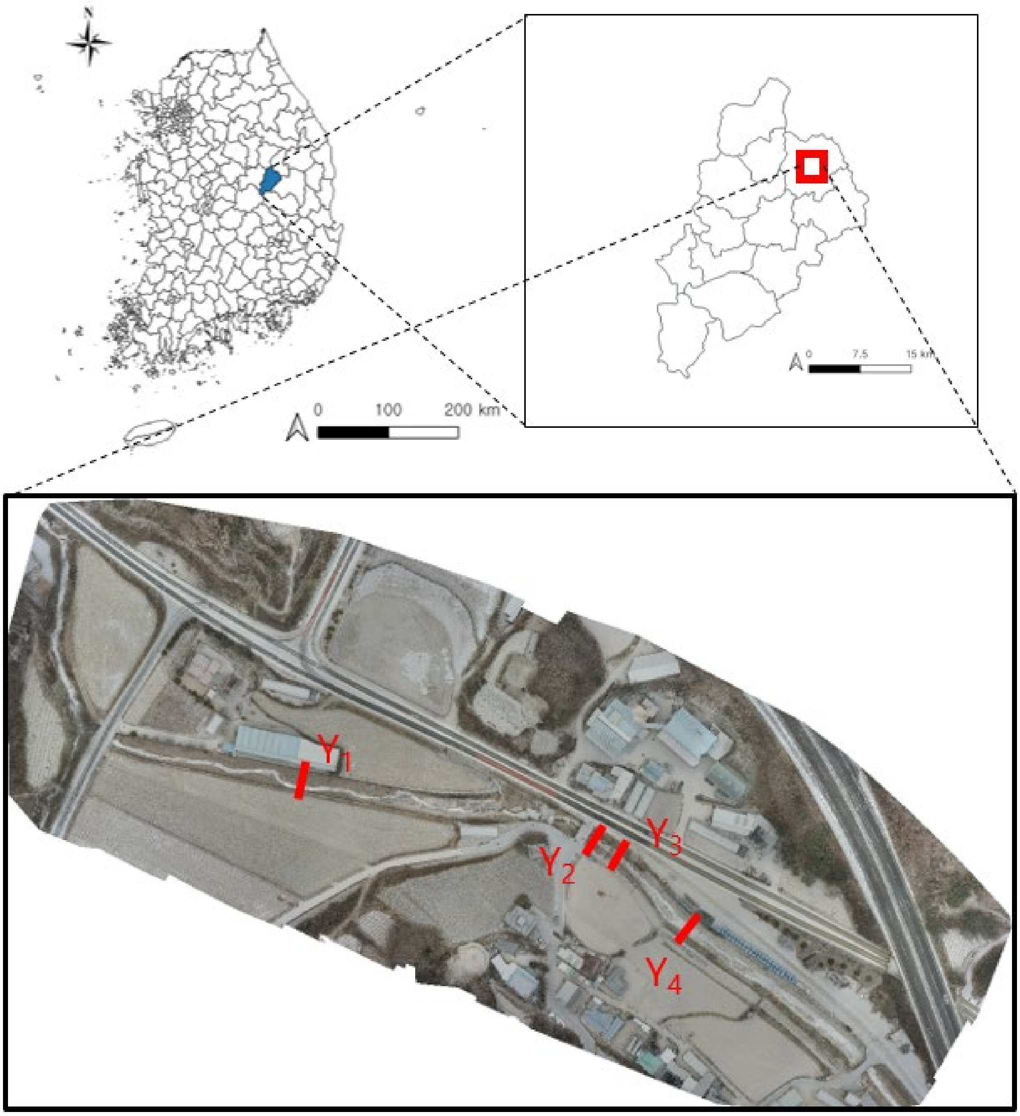

Figure 23. Study area of the applied stream, Pori-cheon stream in Yecheon-gun (Blue area in the top left panel) South Korea. The aerial image is taken and produced by the authors and no copyright is required.

https://doi.org/10.5194/gmd-2023-57
Preprint. Discussion started: 27 June 2023

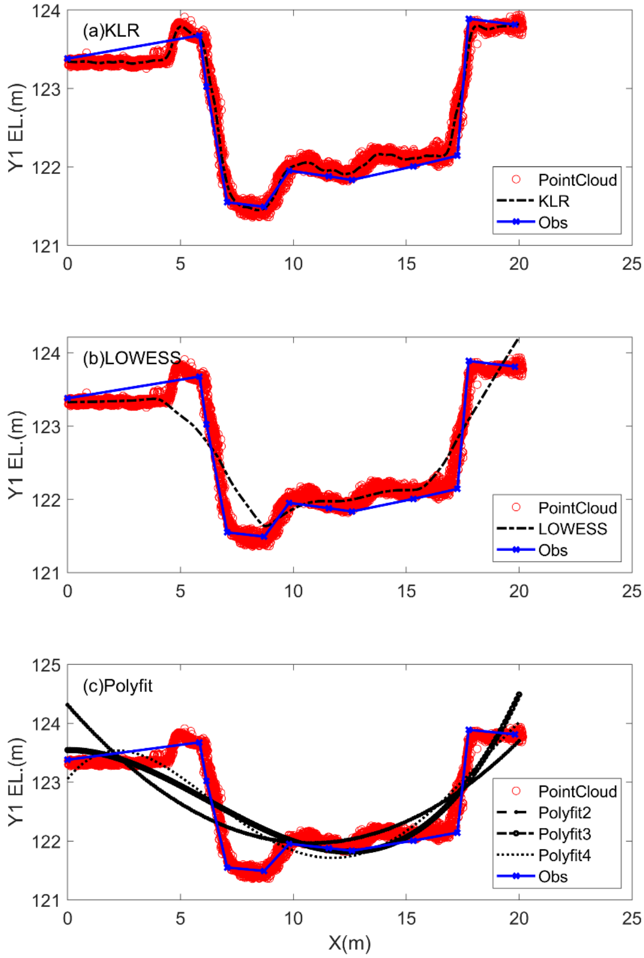

Figure 24. Point cloud data (red circles) for the Y_1 of Yecheon site and model-fitted line (black dashed line) with KLR (panel(a)), LOWESS (panel(b)), and PolyFit (panel(c)) as well as the ground surveying (blue solid line with x marker).

https://doi.org/10.5194/gmd-2023-57
Preprint. Discussion started: 27 June 2023

Geoscientific Model Development Discussions

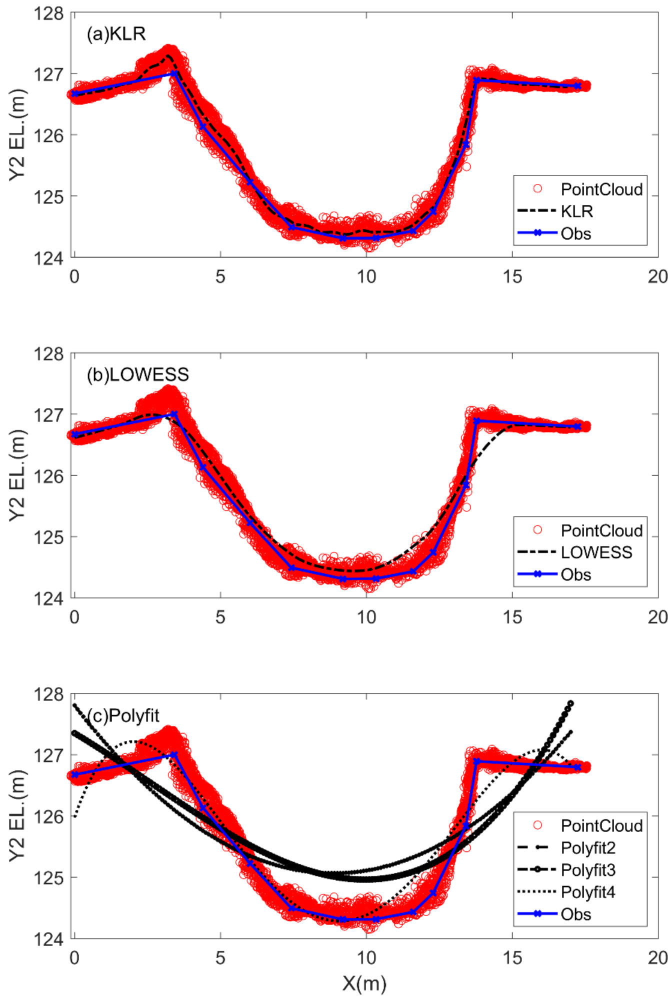

1050

1051 Figure 25. Point cloud data (red circles) for the Y_2 of Yecheon site and model-fitted line (black
1052 dashed line) with KLR (panel(a)), LOWESS (panel(b)), and PolyFit (panel(c)) as well as the
1053 ground surveying (blue solid line with x marker).

Geoscientific Model Development Discussions
Open Access
EGU

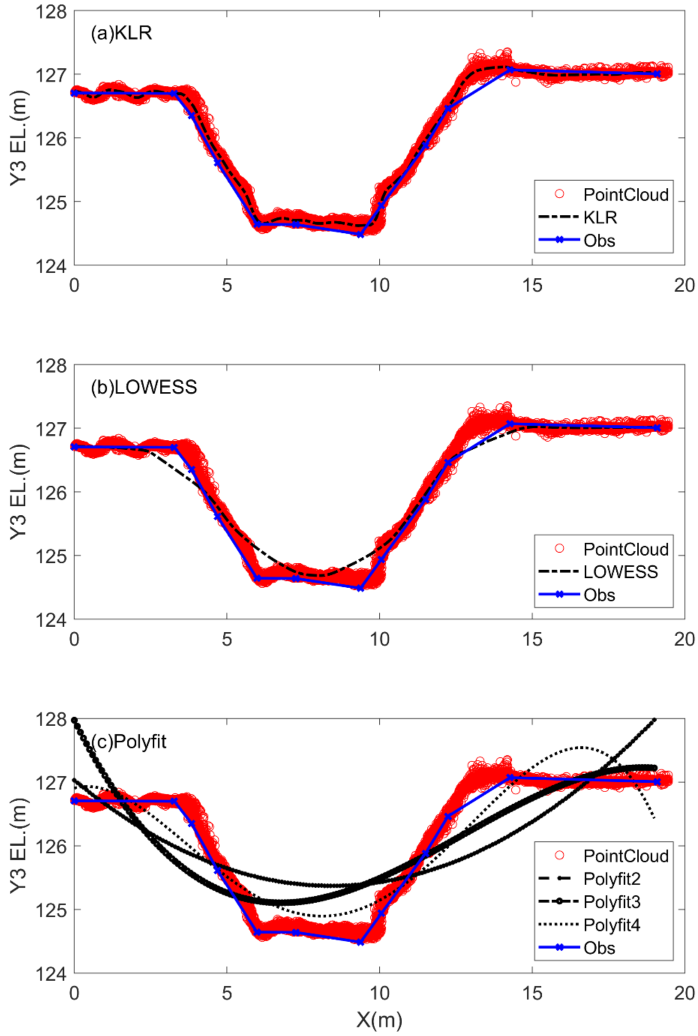

1054

1055 Figure 26. Point cloud data (red circles) for the Y_3 of Yecheon site and model-fitted line (black
1056 dashed line) with KLR (panel(a)), LOWESS (panel(b)), and PolyFit (panel(c)) as well as the
1057 ground surveying (blue solid line with x marker).

1058

https://doi.org/10.5194/gmd-2023-57
Preprint. Discussion started: 27 June 2023

Geoscientific Model Development
Discussions

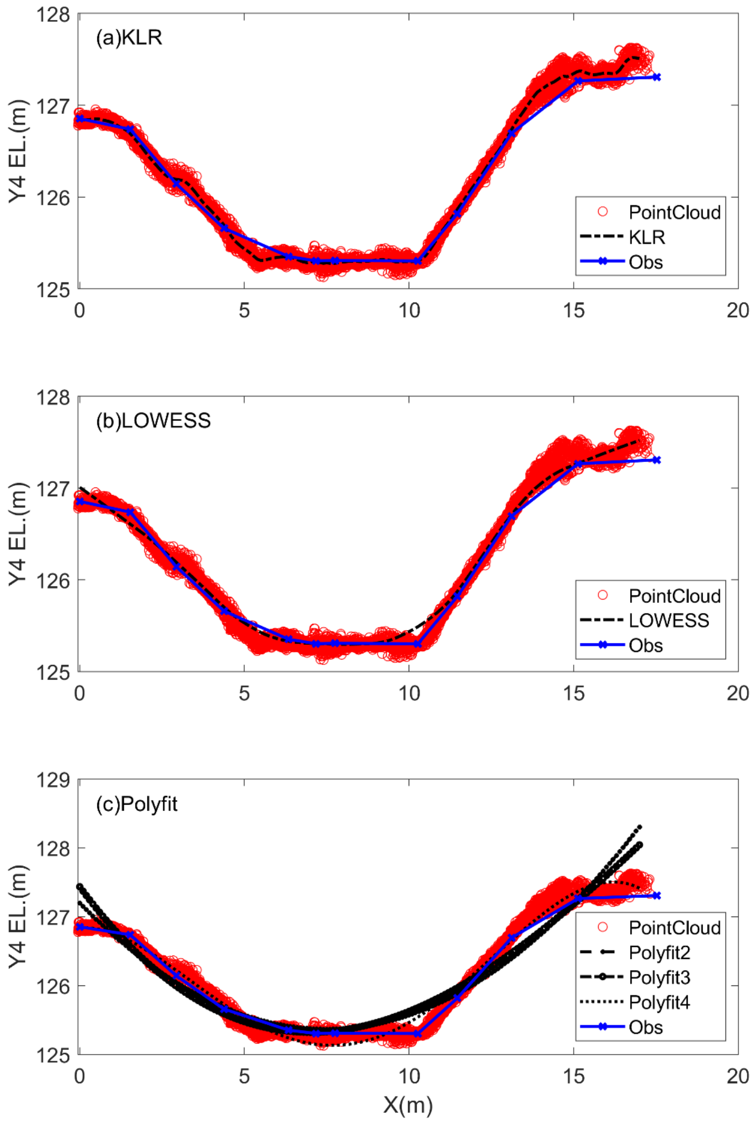

1059

1060 Figure 27. Point cloud data (red circles) for the Y_4 of Yecheon site and model-fitted line (black
1061 dashed line) with KLR (panel(a)), LOWESS (panel(b)), and PolyFit (panel(c)) as well as the
1062 ground surveying (blue solid line with x marker).

1063
1064